Available online at www.sciencedirect.com
ScienceDirect
Geochimica et Cosmochimica Acta 70 (2006) 5035–5060
Geochimica
www.elsevier.com/locate/gca

Laboratory condensation of refractory dust in protosolar and circumstellar conditions

Alice Toppani [a,b,*], Guy Libourel [a,c], François Robert [b], Jaafar Ghanbaja [d]

[a] Centre de Recherche Pétrographiques et Géochimiques – CNRS UPR2300, 15 rue Notre Dame des Pauvres, BP 20, 54501 Vandoeuvre-les-Nancy, France
[b] Laboratoire d'Etude de la Matière Extraterrestre – CNRS UMS2679-Muséum National d'Histoire Naturelle, 61 rue Buffon, 75005 Paris, France
[c] Ecole Nationale Supérieure de Géologie, INPL, BP40, 54501 Vandoeuvre-les-Nancy, France
[d] Service Commum de Microscopie Electronique à Transmission Faculté des Sciences – Université Henri Poincaré, Nancy I, BP 239, 54506 Vandoeuvre-les-Nancy, France

Received 15 February 2005; accepted in revised form 24 May 2006

Abstract

In order to better understand condensation processes that took place in the solar nebula and to evaluate the effect of kinetics on the condensed matter, we have built an experimental apparatus for studying condensation of multi-elemental refractory gases at high-temperature and low-pressure. The condensation of a Mg–Si-rich gas, with solar interelement ratios of Ca, Al, Mg and Si, and of a Ca–Al-rich gas under a total pressure of $\sim 4 \times 10^{-3}$ bar at temperatures from 1045 to 1285 °C and for run times of 4–60 min results in direct formation of crystalline oxides or silicates such as corundum, spinel, anorthite, melilite, Al-diopside, forsterite and enstatite. The mineralogy of the condensates, close to that predicted at equilibrium, varies with the duration of an experiment and the temperature of condensation. The chemical reactions between gas and condensates are rapid enough to attain a steady state in less than one hour. The condensation results in chemical fractionation of the gas, i.e. a depletion of the gas in refractory elements at high temperature. Finally, besides revealing the textures of refractory crystals, which condense from a gas of complex chemical composition, this study shows that certain phases, such as spinel, have favored kinetics of condensation. Our experimental results confirm that refractory inclusions in primitive meteorites could have formed by condensation from a hot nebular gas. Similarly, we confirm that crystalline grains can condense at high temperature in the outflows of evolved stars. In both cases, our results indicate that kinetic processes certainly influence grain mineralogy. Kinetic processes must thus be taken into account in modeling the pressure-temperature conditions of circumstellar environments.

1. Introduction

Variations of properties (e.g., chemical composition, density) of the solar system planets have been early related (Urey, 1952) to the fractionation of elements during the condensation of a cooling nebular gas in a radially stratified protosolar nebula, with temperature and pressure decreasing with heliocentric distance (e.g., Lewis, 1974). In such models, elements became incorporated into solid nebular material depending on their thermodynamic stability during the condensation of grains from the gas. While the variations of chemical properties of rocky bodies with heliocentric distance are not firmly established, it is nevertheless evident that condensation has played an important role in establishing the chemical compositions of meteorites (e.g., Larimer, 1967; Palme, 2000). Although it is difficult to ascertain a condensation origin for each component of primitive meteorites, some, such as the Ca–Al-rich inclusions (CAIs), the oldest objects of our solar system (e.g., Gray et al., 1973; Amelin et al., 2002), seem to be good candidates. Indeed, their composition, markedly enriched in refractory elements relative to the solar gas, matches that of the material calculated to have condensed at equilibrium

* Corresponding author. Present address: Centre de Spectrométrie Nucléaire et de Spectrométrie de Masse, Bât. 104, 91405 Orsay Campus, France.
E-mail address: toppani@csnsm.in2p3.fr (A. Toppani).

0016-7037/$ - see front matter © 2006 Elsevier Inc. All rights reserved.
doi:10.1016/j.gca.2006.05.020

at very high temperature from a cooling solar gas (Lord, 1965; Larimer and Anders, 1970; Grossman, 1972). Furthermore, it was also suggested by thermodynamic calculations that their peculiar mineralogy (e.g., Christophe Michel-Lévy, 1968; Grossman, 1975; MacPherson, 2004) results from condensation processes (e.g., Larimer and Anders, 1970; Marvin et al., 1970; Grossman, 1972).

A gas-to-solid condensation origin (Gilman, 1969; Fix, 1970; Lattimer et al., 1978; Sharp and Wasserburg, 1995; Lodders and Fegley, 1997; Ebel, 2000; Toppani et al., 2005) has also been attributed to the interstellar dust, which is mainly formed in the outflows of red-giant or supernovae stars (Woolf and Ney, 1969; Gehrz, 1989). This interstellar dust plays a fundamental role in the physics (e.g., heat transfer) and chemistry of the interstellar medium (ISM), in the chemical evolution of the galaxy and in the formation of stars.

Condensation processes which are thought to result in the main chemical differences between the gas and solids in the galaxy (Field, 1974; Savage and Sembach, 1996) are thus major mechanisms that control the cycle of dust from evolved stars to planetary systems (Tielens and Allamandola, 1987). However, they are still poorly understood today. Indeed, while theoretical models of nucleation or grain growth are lacking experimental data (e.g., Blander and Katz, 1967; Salpeter, 1977; Cameron and Fegley, 1982; Sedlmayr, 1989), the equilibrium thermodynamic modeling of the chemical composition of the grains does not take into account the effects of kinetics (e.g., nucleation or rates of chemical reactions with the gas) (e.g., Fegley, 2000). Laboratory condensation experiments are thus required in order to provide information about the crystallinity, texture or chemical composition of the matter condensing from a solar gas (Toppani et al., 2005).

While nucleation and growth of simple metal or H_2O grains from a gas have been extensively studied for application in atmospheric or material sciences (e.g., Hirth and Pound, 1963; Seinfeld and Pandis, 1998), condensation of more complex vapor, such as the solar gas, is poorly constrained (e.g., Nuth and Donn, 1982, 1983). Indeed, while a few experiments have been performed in non-equilibrium and/or low-temperature conditions (e.g., Arrhenius and Alfvén, 1971; Day and Donn, 1978; Stephens and Kothari, 1978; Nuth et al., 2000) or with non-solar gas (e.g., Nagahara et al., 1988), none of these attempts was able to simulate the astrophysical conditions for condensation of a solar gas because of the difficulty in (1) producing a multi-elemental refractory gas of controlled composition and (2) condensing it at equilibrium and at high-temperature.

In this paper, we report the first successful near-equilibrium laboratory condensation of refractory oxide and silicate minerals (enstatite, forsterite, Al-diopside, melilite, anorthite, spinel and corundum) at high-temperature (~1300–1550 K) and low-pressure ($\sim 4 \times 10^{-3}$ bar) from two different multi-elemental refractory gaseous systems, with one being close to the solar composition with respect to Ca, Mg, Al and Si. These experiments give insights into the process of condensation of a multi-elemental refractory gas under astrophysical conditions, and notably on the effects of kinetics. In addition, they help to constrain the formation conditions of potential nebular condensates, such as the CAIs as well as those of interstellar dust.

2. Experimental method

In order to simulate the condensation of gases in nebular conditions, we have developed a new apparatus, in which condensation experiments from a multi-elemental refractory gas can be performed at low pressure, high-temperatures, and variable oxygen fugacities or run times.

2.1. Experimental design

The new condensation apparatus (Fig. 1) consists of a high-vacuum reaction chamber (Fig. 1a) into which a mixture of gases (CO_2, Ar, He, CO...) can be introduced. Vacuum is achieved using a primary pump and a turbomolecular pump (pressure down to 10^{-9} bar). In this study, experiments were performed in a static vacuum mode at a total pressure of $\sim 4 \times 10^{-3}$ bar of CO_2 or Ar background gas. A baratron gauge was controlling the pressure during the course of all experiments (Toppani et al., 2004, 2005).

Two main processes occur in the reaction chamber: (1) gas production and (2) gas condensation. The production of a multi-elemental refractory gas with a constant composition over time is achieved using a pulsed Nd-YAG laser (1064 nm), which ablates a spinning glass target located at the bottom of the reaction chamber. The laser (~10 mJ, frequency 10 Hz, and pulse duration ~7 ns) is focused on a ~0.2 mm^2 area yielding about ~1 mg/h of ablated material. In addition to allowing an accurate control of the gas composition, the use of a glass target ensures the lack of crystals in the cloud of ablated material. Condensation of the gas occurs at controlled temperature in a platinum furnace located ~18 mm above the target and lined with an alumina tube (Fig. 1a). The alumina lining was essential to achieve a good thermal homogenization of the furnace. Because the investigated temperatures are well below melting temperature of alumina (~2100 °C), it is unlikely that the alumina lining will affect the partial pressure of aluminum. The furnace was designed to have a negative temperature gradient from bottom to top in order to avoid a cold condensation point (Fig. 1b). Measured temperatures decreased from furnace bottom to target surface almost linearly.

2.2. Starting material

Most experiments were performed using a glass with Ca, Al, Mg and Si interelement ratios close to solar (Anders and Grevesse, 1989), hereafter referred to as Mg–Si-rich glass. Other experiments were done using an $An_{50}Di_{50}$ glass (Table 1). The Mg–Si-rich glass was chosen to produce a

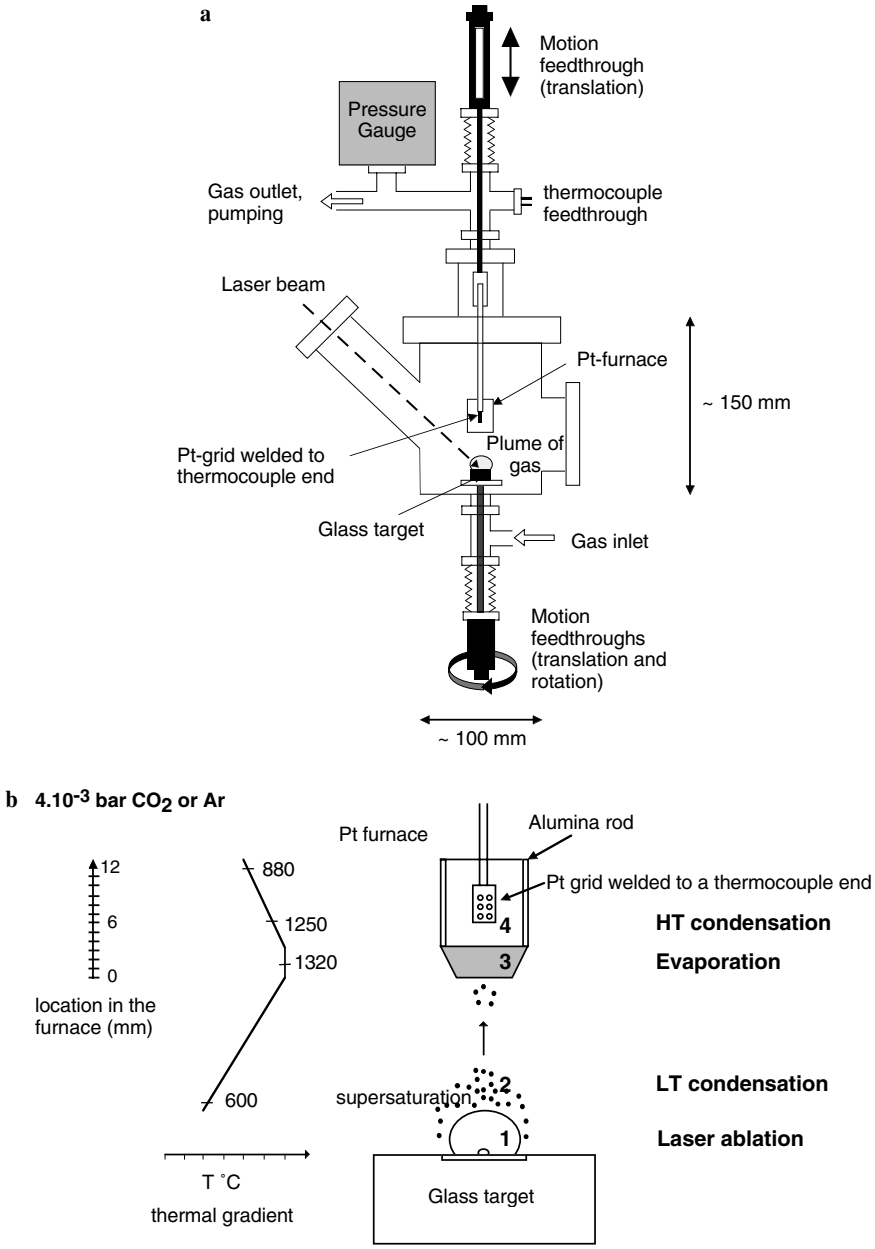

Fig. 1. Sketch of the experimental design (not to scale). (a) General scheme of the device. The Pt-furnace is lined with an alumina tube of about 12 mm of height and 3 mm of interior diameter. Distance between the target and furnace is about 18 mm. (b) Scheme showing the experimental procedure. The reaction chamber is divided into four different zones (laser ablation, low-temperature condensation, evaporation and high-temperature condensation zones, see text for explanation). Condensates are collected on the Pt-grid welded to the end of a Pt–Rh_{10} thermocouple. The condensation temperature (T_c), defined as the Pt-grid temperature (±20 °C), was monitored during each experiment. Note that the schematic temperature gradient is given for a condensation temperature of 1250 °C.

Table 1
Composition (wt%) of the starting material

Starting material	MgO	Al_2O_3	SiO_2	CaO	Total	Mg/Si	Al/Si	Ca/Si
Mg–Si rich glass	36.1	4	56.9	3	100	0.94	0.08	0.06
$An_{50}Di_{50}$	9.3	18.7	48.6	23.4	100	0.29	0.45	0.52
Solar gas[**]	38.9	3.9	54.1	3.1	100	1.07	0.08	0.06
CAIs[a]	10.2	29.6	29.1	28.8	97.7[*]	0.52	1.2	1.06
CAIs[b]	13.1	26.6	33.7	21.6	95[*]	0.57	0.93	0.68

[a] From MacPherson et al. (1988) and references therein, Type B1 CAIs (average of 12 microprobes analyses).
[b] From MacPherson et al. (1988) and references therein, spinel-rich fine-grained inclusions (bulk analyses).
[*] Elements such as Ti, Fe and Na are present in minor proportions (<2 wt%).
[**] Compositions recalculated for solar gas containing only Ca, Al, Mg and Si elements (Anders and Grevesse, 1989).

gas, which will be considered, in the following, as a proxy of the solar gas whereas the $An_{50}Di_{50}$ was used to produce a more Ca–Al-rich gas (see composition in Table 1). Glasses were synthesized from mixtures of reagent grade oxides (SiO_2, Al_2O_3, MgO) and carbonates ($CaCO_3$), twice fused in air at 1600 and 1400 °C for the Mg–Si-rich and $An_{50}Di_{50}$ compositions, respectively. Parallelepipeds of glass were sliced and abraded in order to improve laser absorption at 1064 nm. Mg–Si-rich glass was difficult to quench without partial recrystallization. Therefore, only the near-surface portion of the glass slabs was ablated in order to ensure the absence of crystallites in the ablated material. Compositions and homogeneities were checked using the Cameca SX50 electron microprobe at "Service Commun de Microanalyses" of the Henri Poincaré University, Nancy, France.

2.3. Experimental procedure

The primary gas produced by laser-ablation of the glass target is not condensed directly at high-temperature. To ensure condensation of the multi-elemental refractory gas at high-temperature, a four step experimental design was adopted, each step corresponding to a zone in the reaction chamber (Fig. 1b). The first step consists in the laser-ablation of the glass target in zone 1. Then, amorphous nanoparticles of glass target composition form in zone 2 from the "primary" gas produced in zone 1. Following the preferential direction of the laser plume, these particles are swept into zone 3. In zone 3, a secondary gas is produced by evaporation of the nanoparticles. Finally, this gas condenses in zone 4 at a controlled temperature and for different run times. Each step is described in detail below.

2.3.1. Steps 1 and 2: Low-temperature non-equilibrium condensation

Calibration experiments were performed in order to study the formation of nanoparticles in zone 2 (chemical composition, morphology, crystallinity of nanoparticles, etc.). For this purpose, horizontal steel plates were placed ~4 mm above the target (and below the furnace), and a mixture of two types of products was collected: (1) fluffy aggregates of ~10 nm-sized amorphous nanoparticles and (2) large amorphous droplets (50 nm to 2 μm) (Fig. 2).

(1) At the relatively high total pressure of $\sim 4 \times 10^{-3}$ bar, the hot laser-ablated gas (zone 1 in Fig. 1b) expanding in the cold background gas is rapidly supersaturated in zone 2. This leads to the condensation of neutral and ionized species of the laser-ablated gas above the target and the production of nanoparticles (Fig. 2) (Abraham, 1974) in agreement with observations from pulsed laser deposition techniques (e.g., Chen, 1994; Gnedovets et al., 1996; Marine et al., 2000). In our design, this non-equilibrium low-temperature condensation of nanoparticles occurs between 25 and 630 °C, depending on the temperature gradient induced by the Pt-furnace.

(2) The large amorphous droplets (Fig. 2) are material ejected as liquid, directly from the heated glass target sub-surface and will be referred as laser-ablation droplets. Note that their formation by condensation of liquid is ruled out because their presence is observed at any temperature and at any total pressure (down to 10^{-6} mbar in total pressure). Rather, their occurrence is very common in pulsed vapor deposition experiments (Chen, 1994) and has been reported around ablation pits in laser ablation ICPMS work (e.g., Wiechert and Hoefs, 1995). Indeed, although most of the laser energy is used to break atomic bonds in the glass, some dissipates at the sub-surface of the glass as heat, which leads to the melting of the sub-surface. Droplets of melt are then ejected from the surface mainly due to the reverse shock resulting from the expansion of the gas plume and are quenched in the low-temperature zone 2. The surfaces of our glass targets were observed by SEM and consistently show features indicating a sub-surface melting.

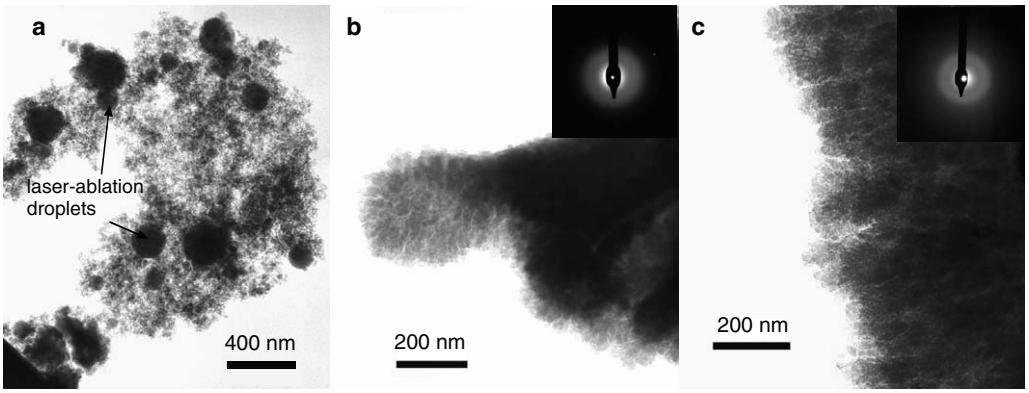

Fig. 2. Bright field transmission electron micrographs of non-equilibrium low-temperature nanoparticle condensates ($\sim 4 \times 10^{-3}$ bar total pressure). (a) Nanoparticles from Mg–Si-rich gas collected at 25 °C. Material from a horizontal collection plate was scratched and deposited on a Cu TEM grid. (b) Nanoparticles from Mg–Si-rich gas collected at 280 °C. (c) Nanoparticles from $An_{50}Di_{50}$ gas collected at 600 °C. For (b and c) nanoparticles were deposited on a vertical Pt-grid which was directly observed by TEM. Black support is the platinum. Diffraction patterns associated with (b and c) micrographs show the amorphous nature of the nanoparticles. Note the absence of significant differences between the nanoparticles condensed from different gases and/or various temperatures.

To provide evidence that the amorphous nanoparticles are not dust particles ejected from the glass during the laser ablation but true condensates from the laser-ablated gas, an experiment has been performed under a total pressure of $\sim 10^{-7}$ bar at a temperature of 25 °C. The TEM observation of the collected products revealed the presence of an amorphous thin film and laser-ablation droplets. Contrary to the previous test experiments performed at 4×10^{-3} bar, the amount of collisions between the ablated species and the ambient gas at 10^{-7} bar is very low, so neither supersaturation of the silicate gas nor condensation of nanoparticles is achieved. As described in thin-film deposition techniques, the observed thin film has grown by the deposition of individual molecules or atoms ablated from the glass target. This experiment clearly shows that the laser ablation of the glass target produces only (1) the gas that subsequently condenses as amorphous nanoparticles and (2) the laser-ablation droplets.

The amorphous nanoparticles were analyzed by transmission electron microscopy energy dispersive X-ray spectroscopy (TEM-EDX). Within analytical error (±20%), they are not chemically fractionated relative to the target composition (Fig. 3). In contrast, the amorphous laser-ablation droplets have compositions chemically fractionated relative to the target, consistent with fractional evaporation, not condensation, of the molten droplets (Fig. 4). Fig. 4 shows that small droplets are more fractionated than larger ones, due to the higher surface/volume ratio of the former.

2.3.2. Step 3: Formation of the secondary gas

The primary gas produced by laser-ablation of the glass target in zone 1 has been "converted" to nanoparticles by homogeneous condensation in zone 2. These nanoparticles (and the laser-ablation droplets) are swept into zone 3 following the preferential flow of the gas plume. To verify the presence of this preferential flow, we collected material on large horizontal plates in zone 2. The amount of material decreases from the center of the plate (right above the plume of gas) to the edge of the plate, which indicates a

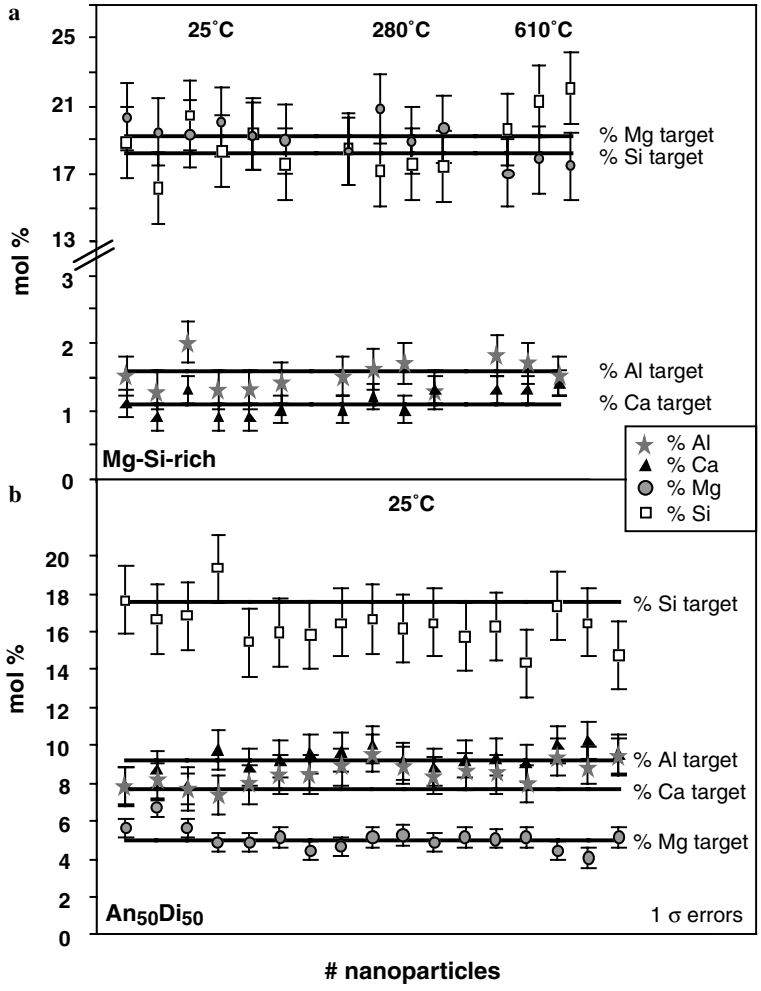

Fig. 3. Chemical compositions of the nanoparticles condensed in zone 2 (Fig. 1) under non-equilibrium conditions compared with that of the target for two starting compositions (Mg–Si-rich glass (a) and $An_{50}Di_{50}$ glass (b)). Chemical compositions of the nanoparticles formed from the Mg–Si-rich gas are given for three temperatures of homogeneous condensation. Nanoparticles were analysed by EDX using TEM (Nancy) whereas glass was analysed by WDS using electron microprobe at Nancy (Université Henri Poincaré).

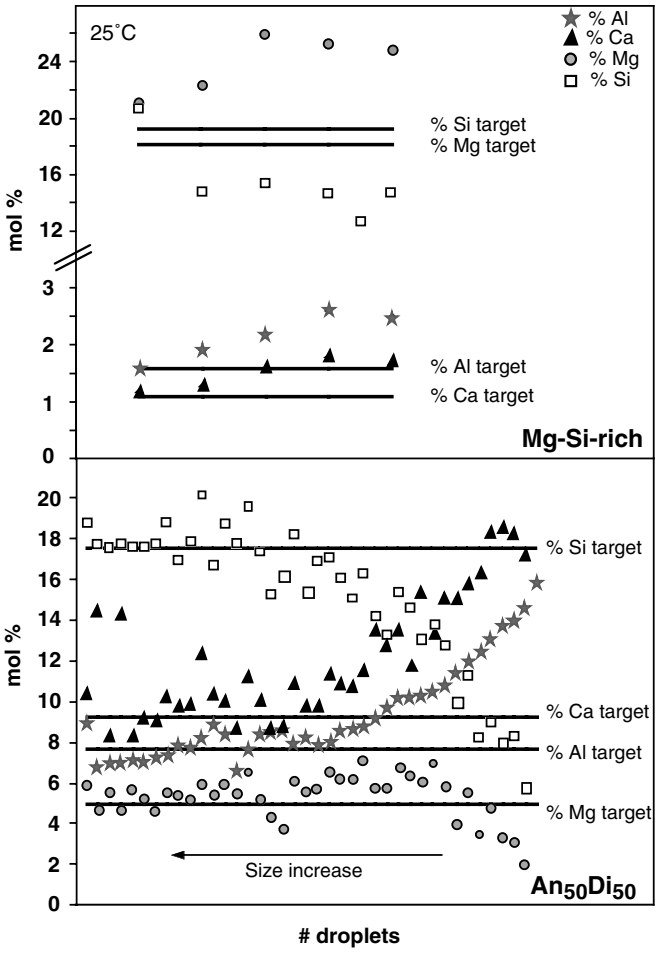

Fig. 4. Chemical compositions of the laser-ablation droplets collected at 25 °C in zone 2 (Fig. 1b) compared with that of the target for two starting compositions (Mg–Si-rich and $An_{50}Di_{50}$ glasses). Note that for the $An_{50}Di_{50}$ composition, laser-ablation droplets were arranged according to their approximate size (from ~300 nm to ~2 μm). Error bars (±8 % of the values) are not reported for clarity.

preferential flow of material transport along the vertical axis of the plume (which is perpendicular to the glass target).

The nanoparticles (of target composition) are evaporated at the bottom of the furnace (zone 3) to produce a secondary gas. In order to determine the temperature regimes that produce secondary gases of the target composition (Table 2), we performed the calibration experiments at evaporation temperatures varying from 950 to 1360 °C. These experiments show that the amorphous nanoparticles entering the highest temperature part of the furnace (~1% of the ablated material) are vaporized (in less than a few seconds) at temperatures lower than the expected volatilization temperature of the corresponding glass target (liquidus temperature of ~1580 °C for the Mg–Si-rich composition, ~1275 °C for the $An_{50}Di_{50}$ composition) resulting in the production of a metastable gas. This low temperature of evaporation (zone 3) mainly results from the nanometric size of the nanoparticles. Indeed, nanoparticles between 1 and 100 nm are in an intermediate state between the solid and the molecular states (Wautelet, 2005). Their physical properties are thus different from those of macroscopic matter because of their extremely large surface/volume ratio. For instance, their melting temperature is known to decrease strongly with decreasing radius (Buffat and Borel, 1976; Wautelet, 2005), down to 30% decrease for 2 nm-sized Ni particles (Qi et al., 2001).

At the evaporation temperature of 982 °C, not all nanoparticles are evaporated in zone 3, so the residue of this partial evaporation was captured and analyzed (Experiment # 346, Table 2). The evaporated residues of the Mg–Si-rich nanoparticles show enrichment of Al and Ca, and depletion in Mg and Si due to the partial evaporative loss of Si and Mg (Fig. 5). At the evaporation temperature of 1015 °C (zone 3), residues of the evaporated nanoparticles were mainly aluminous particles of maximum sizes estimated ⩽1–2 nm (experiment # 343, Table 2). Evaporation of the Mg–Si-rich nanoparticles in zone 3 is thus almost complete at 1015 °C. To ensure the production of a gas of target composition in zone 3 and free of solids >1 nm, all condensation experiments were carried out using an evaporation temperature ⩾1115 °C. However, the presence of some Al-rich nuclei (solids <1 nm) in this gas cannot be completely ruled out since it was not possible to experimentally prove their total disappearance at an evaporation temperature ⩾1115 °C. The $An_{50}Di_{50}$ glass has a lower volatilization temperature than the Mg–Si-rich glass, therefore the $An_{50}Di_{50}$ nanoparticles are also likely to be totally evaporated at a temperature ⩾1115 °C. Fig. 6 summarizes the temperature conditions for which partial and total evaporation take place inside zone 3 of the furnace. Note that the use of this nanoparticle evaporation strategy has eliminated a possible influence of the laser and of the ionized species present in the laser ablation plume on the condensation process.

An upper limit of $\sim 7 \times 10^{-6}$ bar for the sum of the partial pressures (P_{evap}^{TOT}) of the evaporated gas species (e.g., Ca, Mg, Si, Al and O for the Mg–Si-rich gas) inside the furnace is calculated using the ideal gas law (1300 K, volume of the furnace) for a residence time upper limit of 0.5 s. Assuming that the molecules go through the furnace in a straight vertical path (~3 mm) at a mean velocity of ~1000 m/s (1300 K), a lower limit residence time of 10^{-6} s can be estimated, which corresponds to a pressure lower limit on P_{evap}^{TOT} of $\sim 10^{-11}$ bar.

2.3.3. Step 4: High-temperature condensation

As the hot gas produced in zone 3 moves upward due to the negative furnace temperature-pressure gradient, it slowly cools down and condensation takes place in zone 4 of the furnace. Condensates were collected at the top of zone 4 on a vertical Pt-grid welded to the end of a $Pt–Rh_{10}$ thermocouple (Tissandier et al., 2002). Although condensation could occur in the entire zone 4, the condensation temperature (T_c) is defined as the Pt-grid temperature (±20 °C). Because of the high thermal conductivity of the platinum, the Pt-grid is supposed to be relatively homogeneous in

Table 2
Experimental conditions

Type	No.	Location (mm)[a]	Evap Temp.[b]	Cond. Temp.[c]	Run times (min)	Pressure (mbar)	Target	Gas	Major phase found
Calibration	343	6	1015	945	62	5	Mg–Si	CO_2	(Fo, res), Cor
	346	6	982	912	63	4.5	Mg–Si	CO_2	En, Fo, res, Cor
Annealing test	308	6		25 and 1070[d]	52 and 62	5	Mg–Si	CO_2	Fo
	318	0		1040[e]	67	4.5	Mg–Si	CO_2	En, Fo
Formal-$An_{50}Di_{50}$	233	5	1120	1050	61	5.4	$An_{50}Di_{50}$	CO_2	Al-diop, Mel, C_3S
	253	4.5	1215	1145	66	6.5	$An_{50}Di_{50}$	CO_2	Sp, Al-diop, Mel
Formal- Mg–Si-rich	295	6	1115	1045	52	4	Mg–Si	CO_2	En, Fo, Al-diop, Sp, Cor
	304	6	1140	1070	56	4.8	Mg–Si	CO_2	En, Fo, Al-diop, Sp, Cor
	296	6	1165	1095	63	5	Mg–Si	CO_2	Fo, Al-diop, Mel, An, Sp, Cor
	327	6	1210	1140	51	4.5	Mg–Si	CO_2	Al-diop, Mel, An, Sp, Cor, Lar
	297	6	1248	1178	56	5.3	Mg–Si	CO_2	An, Sp, Cor
	305	6	1350	1285	50	5	Mg–Si	CO_2	Sp, Cor
	339	6	1115	1045	13	5.2	Mg–Si	CO_2	Fo, Al-diop, Mel, Cor
	340	6	1208	1138	4	5.5	Mg–Si	CO_2	Fo, Al-diop, C_3S, Mel, An, Cor
	336	6	1209	1139	14	6	Mg–Si	CO_2	Al-diop, Mel, An, Sp, Cor
Formal- Ar gas	267	5.5	1145	1075	65	6	Mg–Si	Ar	Fo, Al-diop, An, Sp, Cor
	341	6	1211	1141	14	4.5	Mg–Si	Ar	Al-diop, Mel, An, Cor
Blank	321	6		925–1077	278	5	Mg–Si	CO_2	Al-diop, Mel, An, Cor, Hib
	285	6		850–1250	300	10	Mg–Si	CO_2	Mel, An, Sp, Cor
	293	6		960–1125	143	7.5	Mg–Si	CO_2	En, Fo, Mel, An, Sp, Cor

En, Fo, Al-diop, Sp, Cor, Mel, Hib, C_3S and Lar stand respectively for enstatite, forsterite, Al-diopside, spinel, corundum, melilite, hibonite, Ca_3SiO_5 and larnite. Res. stands for residue of evaporation. Mg–Si stands for Mg–Si-rich gas.
Notes. phases only found once are not reported in this table except for the short experiments for which only a few analyses have been carried out and for blank experiments.
[a] Distance in mm from the bottom of the 12 mm high furnace (Fig. 1b).
[b] With the exception of experiments # 343 and # 346, evaporation temperatures in °C (zone 3, Fig. 1b) were not measured but estimated from temperature gradients. The temperature gradient were calibrated for different temperatures of condensation.
[c] Temperatures of condensation (zone 4, Fig. 1b) are given in °C (±20 °C). They were measured during the course of experiments.
[d] During this annealing test experiment # 308, nanoparticles condensed at 25 °C were collected during 52 min on a vertical Pt-grid inside a cold furnace and then in the same run, they were heated at 1070 °C during 62 min.
[e] During this annealing test experiment # 318, nanoparticles condensed between 300 and 500 °C were collected on a vertical Pt-grid at the bottom of the furnace at temperature of 1040 °C during 67 min.

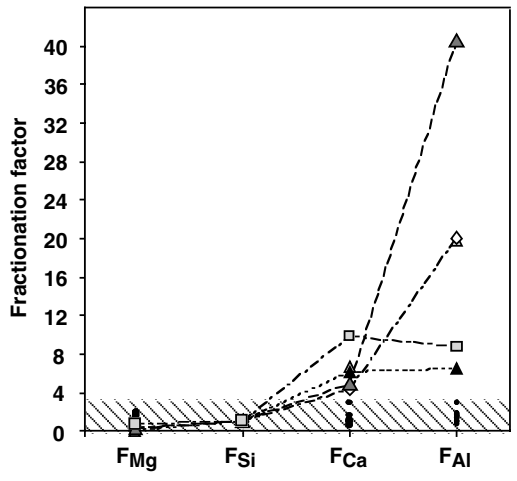

Fig. 5. Chemical fractionation of evaporation residues from the 982 °C evaporation temperature experiment (# 346) normalized to Si and to the Mg–Si-rich glass target composition (fractionation factor $F_X = (X/Si)_{sample}/(X/Si)_{initial}$). The four symbols stand for four different analyzed residues. Residues in the hatched zone are almost unfractionated relative to the target. Some corundum grains with no silicon enrichment (F_x not calculated) were also found among these evaporation residues.

temperature and in thermal equilibrium with the surrounding gas. In addition, the large size of the grid relative to that of the furnace (2.5 mm width, 3 mm height compared to 3 mm diameter, ~9 mm height, respectively) tends to decrease the vertical thermal gradient and homogenize the gas temperature around the Pt-grid. The Pt-grid was always located in the middle of the furnace in order to optimize the range of explored temperatures of condensation (Fig. 6). Although slightly variable from one experiment to another, the estimated thermal gradient between the evaporation zone 3 and the Pt-grid was about 70 °C. The radial thermal gradient across the furnace was about 20 °C.

The systematic observation of amorphous laser-ablation droplets on the Pt-grids at the end of high-temperature experiments indicates that they were not completely evaporated while being in the furnace (zones 3 and 4). Their EDX analysis shows evidence for evaporation with depletion in magnesium and to a lesser extent, in silicon accompanied by enrichments in Ca and Al (Fig. 7). Their abundance was observed to increase with the duration of the experiment and the furnace temperature. An increase in the furnace temperature induced an increase of the tem-

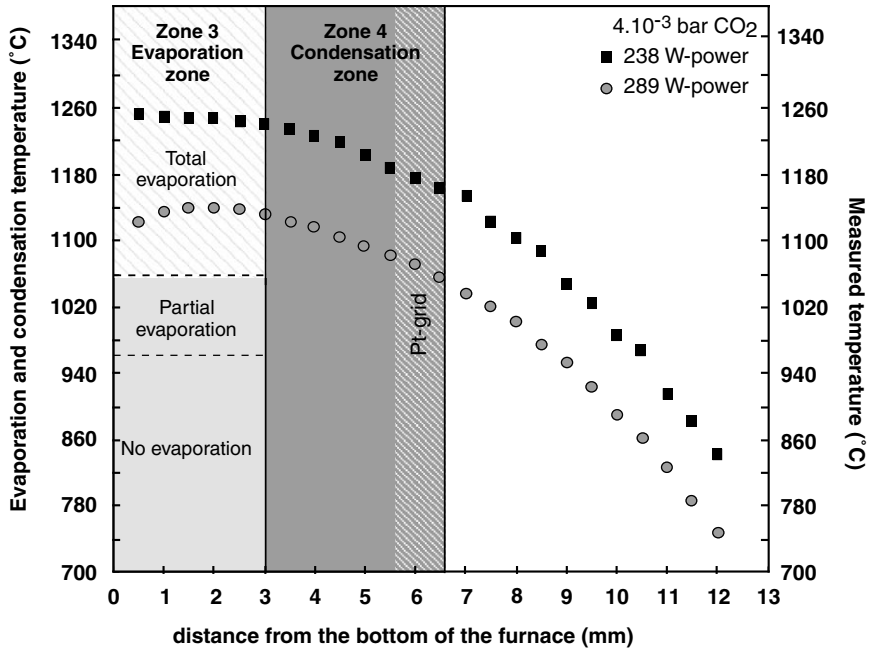

Fig. 6. Temperature gradients and processes occurring inside the furnace (evaporation of the nanoparticles and condensation) during condensation experiments. The two temperature gradients were measured in the furnace heated at different temperatures, i.e. for different power levels (given in watts). It is expected that, during the experiments, the Pt-grid slightly homogenizes the temperature gradient inside the furnace. Temperature ranges given for the zones of partial and total evaporation of the nanoparticles are approximate. All condensation experiments were performed with evaporation temperatures (zone 3) in the regime of total evaporation. Note here that in the regime of total evaporation, Al-rich nuclei (<1 nm) may be still present in the gas.

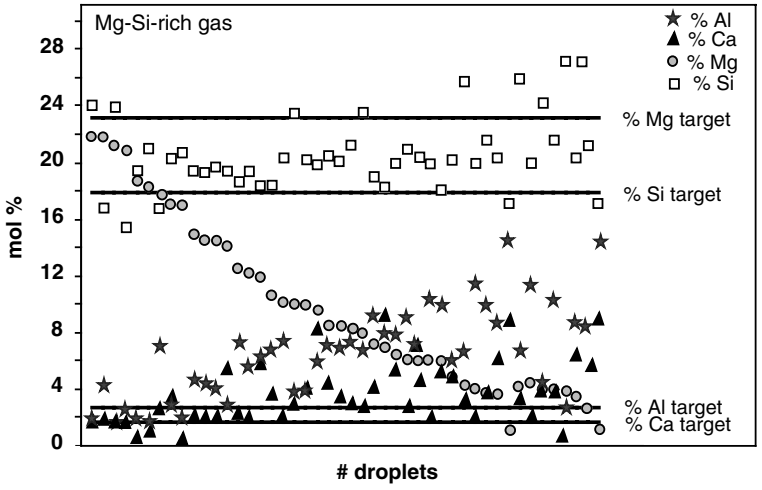

Fig. 7. Chemical composition of laser-ablation droplets collected on Pt-grid in zone 4 (Fig. 1) after 1-h condensation experiments of Mg–Si-rich gas performed at various temperatures (from 1045 to 1285 °C) and run times (from 4 to ~60 min). Laser-ablation droplets are arranged according to their Mg-contents. The observed correlated MgO decrease and Al_2O_3 and CaO increase indicates evaporation. For clarity, error bars (±8 % of the values) are not shown.

perature of the surface glass-target due to radiative heating. As the production of the laser-ablation droplets is related to the melting of the sub-surface target, very high furnace temperature resulted in an increased production of laser ablation droplets. In order to optimize the amount of deposited matter on the Pt-grid relative to the amount of laser-ablation droplets, experiments lasted between 4 to 60 min and were performed at temperatures below 1300 °C (T_c). In addition, experiments showing more than 10% by volume of laser-ablation droplets were discarded. We estimated that evaporation of laser ablation droplets did not change the concentrations of Mg and Si in the gas by more than 10%, even in the worst conditions resulting in both a high abundance of laser-ablation droplets and a high amount of evaporation (50% for Mg).

2.4. Experimental conditions

In each experiment, the reaction chamber was pumped and filled with CO_2 or Ar at the desired pressure after

the insertion of the Pt-grid inside the furnace and installation of the glass target at the bottom of the reaction chamber. Then, the Pt-furnace was slowly heated until thermal equilibrium was reached in order to avoid any rupture in the Pt-furnace. Even at such treatment, the rupture of the Pt-grid usually occurred around 1300 °C (T_c). Temperature was monitored using the thermocouple welded to the Pt-grid. Laser ablation of the glass target started once thermal equilibrium of the furnace and of the Pt-grid was reached. Each experiment was quenched (~2000 °C/min) in a few seconds by (1) ending the laser-ablation, (2) shutting off the power of the furnace and (3) removing the Pt-grid from the furnace using the translation motion feedthrough (Fig. 1a). The Pt-grid was subsequently removed from the thermocouple and recovered for analysis. In the following, we call "condensation time" the duration of an experiment, i.e. the duration of ablation. Before each experiment, the Pt-furnace was chemically cleaned using hot hydrofluoric acid (100 °C) followed by several washings in hot hydrochloric acid and finally water (~100 °C). Alumina linings were replaced before each experiment.

Most condensation experiments were performed in the CO_2 carrier gas, at oxygen fugacity ranging from ~–6 to ~–8 log units, at temperatures between 1045 to 1280 °C and with run times between 4 and 60 min. Some experiments were performed under more reduced conditions using argon as the background gas. The conditions of these four-steps condensation experiments, hereafter referred to as formal experiments, are listed in Table 2. They are also shown in Fig. 6, which summarizes experimentally explored temperatures of evaporation and condensation in the furnace. In addition, test experiments were conducted to demonstrate that the run products of the formal experiments were true condensates (annealing test experiments and blank experiments, Sections 4.2 and 4.4). Their conditions are also listed in Table 2.

Pt-grids or condensed material were studied by a 200 keV TEM (Phillips CM20) at the Henri Poincaré University, Nancy, France. Grains were examined using brightfield and darkfield imaging. Grains compositions were measured using EDX spectroscopy. X-ray thin-film correction procedure (Cliff and Lorimer, 1975) was used. Experimental X-ray correction factors (*K*-factors) were derived from ultra-thin standard minerals and glasses. Crystal structure of the grains was determined by selected area electron diffraction.

3. Results

TEM observations revealed the presence of crystalline phases and few amorphous laser-ablation droplets on the Pt-grids in formal experiments under all explored conditions (Table 2). Although TEM work was difficult to perform on these condensates, our set of experiments (about 40 crystals probed per sample except for short run times where only 15–20 crystals were probed) allows good estimates of the influence of condensation temperature and gas composition on the mineralogy of the condensed crystals to be made. The evaluation of the time-dependence is less accurate because of the difficulties in analyzing tiny and scarce crystals dispersed on the Pt-grids in the shortest experiments (4 min). Note that the possible effects of minor variations in total pressure have been neglected in this study. Although TEM analyses are semi-quantitative, our data set provides information about the variations of chemical composition of the condensed phases as a function of time, temperature and gas composition. Because diffraction work was difficult to perform on the fairly thick (~15 μm) and irregular homemade TEM Pt-grids, only few diffraction data were collected together with chemical analyses on the same crystal.

3.1. Influence of the experimental parameters on the mineralogy of condensed crystals

As most experiments were performed using Mg–Si-rich gas, the effects of temperature, time and oxygen fugacity on the mineralogy of condensed crystals were evaluated for this gas composition. The results of the $An_{50}Di_{50}$ gas condensation are used to study the effect of the gas composition on the mineralogy.

The condensation of the Mg–Si-rich and $An_{50}Di_{50}$ gases at various temperatures and run times resulted in the formation of different phases, namely, enstatite, forsterite, Al-diopside, melilite, anorthite, spinel, corundum and more rarely, larnite and Ca_3SiO_5 (C_3S).

3.1.1. Influence of time

The duration of condensation affects the mineralogy of the condensates. The effect of time was studied at the condensation temperature of ~1140 °C (Tables 2 and 3). The condensate mineralogy changes as run time increases from 4 to 14 min, and then remains the same as run time increases up to 51 min. Short run time of 4 min results in the occurrence of C_3S and the lack of spinel or larnite compared to the condensates produced in the 14 or 51 min runs. At temperature of 1045 °C, similar changes can be observed, with the occurrence of melilite, and the absence of spinel and enstatite in the 14 min run.

3.1.2. Influence of temperature

Our results (Tables 2 and 3) show that the mineralogy of the condensates varies with temperature. The effect of temperature was studied for the longest run times, i.e. around 50–60 min (Tables 2 and 3). The presence of Mg, Si-rich silicates at low-temperature (e.g., enstatite and forsterite at 1045 °C) along with that of only Al-rich oxides at high-temperature (1280 °C) clearly shows that the refractory character of the condensates increases with the temperature of condensation. In addition, except for spinel and corundum condensing over the entire range of experimental temperatures, different phases are present in defined temperature ranges (e.g., melilite was only found in the 1095 °C–63 min and 1140 °C–51 min experiments # 296

Table 3
Distribution of the phases in condensation experiments of Mg–Si-rich and $An_{50}Di_{50}$ gases at $\sim 4 \times 10^{-3}$ bar of CO_2 for different temperatures and run times

Expt	295	304	296	327	297	305	339	340	336	233	253	267	341
Gas	MgSi	MgSi	MgSi	MgSi	MgSi	MgSi	MgSi	MgSi	MgSi	AnDi	AnDi	MgSi[a]	MgSi[a]
Run time (min)	52	56	63	51	56	50	13	4	14	61	66	65	14
Temperature (°C)	1045	1070	1095	1140	1178	1285	1045	1138	1139	1050	1150	1075	1141
Enstatite	X	X										(X)	
Forsterite	X	X	X		(X)?		(X)	X				X	
Al-diopside	X	X	X	X			X	X	X	X	X	X	X
Melilite			(X)	X			X	XX	X	X	X		X
Anorthite			X	X	(X)			(X)	X			(X)	X
Spinel	X	X	X	X	X	XX			X		X	X	
Corundum	(X)	(X)	(X)	(X)	X	X	X	(X)	X			(X)	X
Ca_3SiO_5								X		X			
Larnite				(X)									

MgSi stands for Mg–Si-rich gas, and AnDi stands for $An_{50}Di_{50}$ gas.
Modal proportions of phases were determined qualitatively by TEM observations: XX stands for a major occurrence of the phase on the Pt-grid, (X) stands for a minor occurrence. In experiment # 297, (X)? stands for a rare occurrence of forsterite (only found on a limited area of the Pt-grid) suspected to be contamination, e.g., annealed nanoparticles that were not well evaporated in zone 3. Phase proportions are more difficult to estimate for short run times (1140 °C–4 and 14 min, experiments # 340, 336) due to the scarcity and tiny size of the crystals sitting on the Pt-grid.
[a] Experiments performed in argon gas.

and #327, respectively, Table 2). Duplicate experiments were performed for 1050 °C < T < 1240 °C and show similar changes.

3.1.3. Influence of the background gas

We found no significant influence of the background gas on the mineralogy of condensate. Experiments performed at slightly more reducing conditions in Ar gas (oxygen fugacity buffered by the oxygen from the target) at 1141 °C–14 min (# 341, Table 2) and 1075 °C–65 min (# 267, Table 2) produced crystals mineralogically similar to those condensed in CO_2 ambient gas.

3.1.4. Influence of gas composition

At similar temperatures and run times, the mineralogy of the condensates is highly dependent upon the gas composition (Mg–Si-rich versus $An_{50}Di_{50}$). For example, at 1050 °C, condensation of the $An_{50}Di_{50}$ gas resulted mainly in the formation of Ca–Al-rich crystals (Al-diopside and melilite or Ca_3SiO_5), while condensation of the Mg–Si-rich gas resulted in the formation of Mg, Si-rich silicates (forsterite and enstatite) in addition to Al-diopside, spinel and corundum (Table 2). The mineralogy of the condensates from $An_{50}Di_{50}$ gas does not significantly change over the explored range of temperatures (1050 °C < T < 1150 °C).

3.2. Size, morphology and texture of the condensed crystals

The condensed crystals are usually evenly distributed on the Pt-grids, and except for some specific textures discussed below, the crystals are not piled up. Crystal size shows wide variation (50 nm up to 4 μm, average size of ~250 nm), with the largest grains having been condensed at highest temperatures. As run duration decreases, the amount of material decreases with crystals becoming smaller (average size of ~40 nm) and more scattered on the Pt-grid (Fig. 8b and f).

The morphology of the condensed crystals varies from euhedral to spherical (Fig. 8) regardless of the compositions of the glass target and background gas (CO_2 or Ar). Al-diopside, forsterite, enstatite, melilite and anorthite crystals show different morphologies from euhedral (Fig. 8h) to completely spherical (Fig. 8a,) whereas spinel and corundum crystals are mainly euhedral (Fig. 8d and e). Few crystallographic defects were observed at the TEM scale, as shown by the diffraction patterns in Fig. 8a–e and g. However, in order to confirm the lack of any defects in the crystals, a more careful TEM or High-Resolution TEM study is needed. The crystals often have a rim of 3–10 nm on their surface (Fig. 8f), which sometimes thickens at the contact with the Pt-support. Darkfield imaging in conjunction with specimen tilting revealed that the rim was amorphous. The presence of such rims is independent on the run time or condensation temperature.

The condensed grains show various textures, from single crystal (Fig. 8a and b) to aggregates of crystals of similar composition (300–500 nm) (Fig. 8i). They also form chains of euhedral crystals (300 nm–>2 μm) of different or similar mineralogy (Fig. 8c and h). Forsterite–forsterite (Fig. 8c), diopside–diopside (Fig. 8h), forsterite–anorthite, melilite–Ca_3SiO_5 or melilite–melilite chains have been observed. A few crystals of the same mineralogy were observed to grow on each other in significantly different orientations (e.g., anorthite, 1140 °C–51 min experiment # 327, Table 2). Spinel and corundum were often observed as plates stacked together, which has been well documented at the highest temperatures in our experiments (Fig. 8e and f). Note that spinel whiskers were observed in the 1285 °C–50 min, Mg–Si-rich gas condensation experiment (# 305, Table 2, Fig. 8e). Their tips also seem to show an amorphous rim of about 10 nm thick.

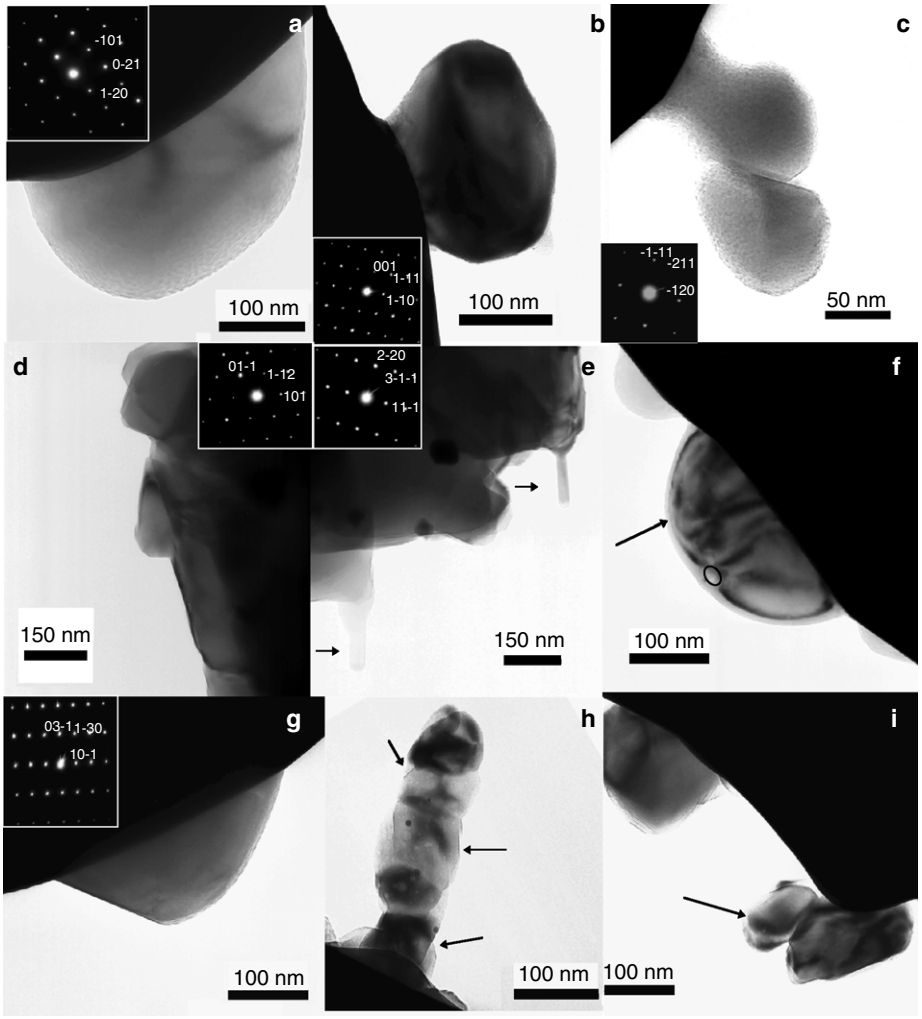

Fig. 8. Bright field transmission electron micrographs of high-temperature condensates (4×10^{-3} total pressure, Mg–Si-rich gas). (a) Single crystal of sub-spherical melilite with its associated diffraction pattern along the [212] zone axis (1140 °C, 51 min, CO_2; Table 2, # 327). (b) Sub-euhedral crystal of Al-diopside (1139 °C, 14 min, CO_2; Table 2, # 336) with its associated diffraction pattern along the [110] zone axis. (c) Two forsterite particles (1070 °C, 56 min, CO_2; Table 2, # 304) with associated diffraction pattern along the [213] zone axis. (d) Large corundum (1285 °C, 50 min, CO_2; Table 2, # 305) with associated diffraction pattern along the [111] zone axis. (e) Large spinel showing two whiskers indicated by arrows (1285 °C, 50 min, CO_2; Table 2, # 305) with associated diffraction pattern along the [112] zone axis. (f) Sub-spherical melilite (1138 °C, 4 min, CO_2; Table 2, # 340) showing an amorphous rim indicated by an arrow. Pit from TEM analyse is also visible (indicated by an ellipse). (g) Anorthite (1178 °C, 56 min, CO_2; Table 2, # 297) with its associated diffraction pattern along the [313] zone axis. (h) Chain of euhedral diopside crystals (1050 °C, 59 min, CO_2; duplicate experiments) showing monoclinic crystallographic shape (indicated by arrows). (i) Crystals of diopside (1070 °C, 56 min, CO_2; Table 2, # 304) showing the late arrival of one of them (indicated by an arrow) on the grid.

3.3. Chemical compositions of the condensed crystals

Variations of chemical composition with temperature, run time, gas composition and oxygen fugacity are described below for each condensed phase. Typical chemical compositions of the phases found in our experiments are reported in Table 4. Care was taken during analyses of single crystals to avoid contamination by adjacent phases when present. Within analytical errors, analyzed crystals are homogeneous with the exception of a few melilites. As the amorphous rims surrounding the condensates were very thin, uncontaminated analyses of their composition were difficult to obtain. In most cases, their compositions were very close to those of the crystals, except for spinel and corundum.

3.3.1. Forsterite

Forsterites from different experiments are stoichiometric ($Mg/Si = 1.93 \pm 0.22 \equiv 2$) within analytical errors, but show aluminum enrichment up to 10 wt% (Fig. 9) independent on the time or temperature of condensation. Because this enrichment does not change the stoichiometry of the crystals, it could be explained by the presence of an Al-rich nanophase such as Al_2O_3. A specific search for such nanophases is required to solve this question. Within detection limits, forsterite does not show any calcium enrichment.

Table 4
Mean compositions of phases observed in selected formal, blank and annealing test experiments of Mg–Si-rich and $An_{50}Di_{50}$ gases at $\sim 4 \times 10^{-3}$ bar of CO_2 for different temperatures and run times

Crystal	Exp	Type	Gas	Nbr	Composition (wt%)*								Range[a]
					MgO	σ	Al_2O_3	σ	SiO_2	σ	CaO	σ	
Enstatite	318	1	Mg–Si	9	37.6	*0.7*	2.6**	*1.6*	58.6	*1.7*	1.2	*1.5*	
	295	2	Mg–Si	2	40.6	*2.0*	1.8	*0.8*	56.9	*1.4*	0.7	*0.2*	
	293	3	Mg–Si	1	35.8	—	2.9	—	58.8	—	2.5	—	
Forsterite	318	1	Mg–Si	3	56.3	*1.2*	0.8	*0.3*	42.3	*0.7*	0.6	*0.3*	
	308	1	Mg–Si	9	55.6	*1.4*	1.3	*0.4*	42.3	*1.4*	0.74	*0.3*	
	304	2	Mg–Si	9	54.0	*2.3*	3.2	*3.0*	42.0	*2.4*	0.8	*0.7*	
	293	3	Mg–Si	5	55.6	*1.7*	1.7	*1.5*	41.6	*2.1*	1.1	*0.4*	
Al-diopside	233	2	$An_{50}Di_{50}$	2	11.0	*1.9*	23.7	*2.8*	40.1	*1.4*	25.2	*0.4*	44.7–53.8 (49.3)
	253	2	$An_{50}Di_{50}$	10	14.6	*1.3*	16.4	*3.5*	46.6	*2.6*	22.5	*1.3*	24.1–46.2 (35.9)
	295	2	Mg–Si	7	16.4	*4.7*	13.7	*5.0*	48.1	*3.3*	21.9	*4.0*	15.9–44.4 (28.9)
	327	2	Mg–Si	11	13.4	*2.1*	16.4	*4.9*	44.6	*4.3*	25.5	*1.7*	19.1–48.0 (34.2)
	321	3	Mg–Si	6	9.1	*3.3*	21.2	*5.8*	44.4	*4.4*	25.4	*4.3*	32.4–70.9 (48.2)
	336	2	Mg–Si	7	11.5	*2.7*	19.7	*5.8*	41.3	*4.9*	27.5	*1.2*	23.3–44.3 (36.2)
Melilite	233	2	$An_{50}Di_{50}$	10	6.9	*1.7*	22.7	*3.2*	32	*2.8*	38.5	*2.0*	29.3–57.2 (43.1)
	253	2	$An_{50}Di_{50}$	4	6.4	*0.2*	25.5	*2.8*	31.9	*4.2*	36.2	*3.2*	36.4–39.2 (38.0)
	327	2	Mg–Si	12	7.4	*3.0*	21.4	*8.9*	32.6	*6.1*	38.6	*1.8*	25.2–87.2 (47.2)
	321	3	Mg–Si	7	4.1	*0.9*	27.8	*3.4*	32.1	*2.7*	36.0	*1.3*	20.5–39.9 (29)
	285	3	Mg–Si	5	2.0	*1.7*	33.2	*2.9*	26.9	*1.2*	37.9	*1.9*	0–24.5 (17)
	340	2	Mg–Si	8	8.8	*4.1*	18.3	*11.3*	35.1	*7*	37.7	*2.1*	16.4–90.4 (55.8)
Anorthite	327	2	Mg–Si	4	1.1	*1.5*	35.1	*1.9*	45.7	*2.5*	18.2	*1.7*	
	293	3	Mg–Si	6	1.8	*1.5*	35.4	*2.2*	44.5	*3.2*	18.3	*1.2*	
Spinel	295	2	Mg–Si	4	27.2	*2.0*	67.4	*3.7*	4.7	*4.2*	0.7	*0.5*	
	305	2	Mg–Si	6	28.8	*1.6*	68.9	*1.2*	1.9	*0.7*	0.5	*0.3*	
	253	2	$An_{50}Di_{50}$	5	29.6	*0.9*	67.4	*1.0*	2.5	*0.8*	0.5	*0.2*	
	285	3	Mg–Si	3	28.2	*0.2*	69.5	*0.9*	1.5	*0.4*	0.7	*0.6*	
Corundum	295	2	Mg–Si	3	3.4	*1.1*	93.6	*4.7*	2.2	*5.4*	0.8	*0.7*	
	305	2	Mg–Si	3	3.2	*2.1*	90.2	*8.4*	5.3	*5.3*	1.3	*1.1*	
	285	3	Mg–Si	2	2.2	*0.8*	95.1	*1.2*	1.5	*1.4*	1.2	*0.6*	
Larnite	327	2	Mg–Si	2	2.2	*1.0*	1.6	*0.4*	36.6	*0.2*	59.6	*1.2*	
C_3S	233	2	$An_{50}Di_{50}$	2	1.4	*0.1*	3.3	*0.7*	19.1	*2.8*	76.2	*2.1*	
Hibonite	321	3	Mg–Si	1	2.2	—	89.2	—	1.3	—	7.3	—	

Analyses were chosen in order to represent the evolution of the chemical composition of the crystal as a function of temperature and type of experiments (blank (3), formal (2) and annealing test (1) experiments). Nbr., gives the number of analyses. Exp., corresponds to the label of the experiment, whose conditions can be found in Table 2. Mg–Si stands for Mg–Si-rich gas.

It is of note that analysed melilite, anorthite or diopside may show a slight depletion of calcium which can be related to sputtering damage by the electron beam during TEM analyses.

[a] Range and means (in parenthesis) of pyroxene or melilite compositions expressed as the content of the Ca–Tschermak ($CaAl_2SiO_6$) end-member in the diposide–enstatite–Ca–Tschermak solid-solution or of åkermanite ($Ca_2MgSi_2O_7$) end-member in the gehlenite–åkermanite solid-solution, respectively.

* Compositions of crystals were obtained by TEM energy dispersive X-ray spectroscopy. Typical precision is about 10%, σ is the standard deviation between the measurements.

** Contents below 2.3 wt% for corundum, below ~1.5 wt% for other phases are subject to caution.

Forsterite condensed in the Ar ambient gas shows the same compositional trend.

3.3.2. Anorthite

Anorthite is stoichiometric within analytical errors. It is enriched in MgO up to 5 wt% (mean around 1.5 wt%) independently on either the time or the temperature of condensation. Anorthite condensed in Ar ambient gas shows the same compositional trend.

3.3.3. Spinel

Spinel has nearly constant Mg/Al ratio of 0.5 but can show enrichments in silica (Fig. 10). Calcium is not enriched in spinel except for the two grains highly enriched in silicon. The deviations from stoichiometry seem to be less pronounced at high temperature. Spinels condensed from the $An_{50}Di_{50}$ gas have about the same chemical compositions as those condensed from the Mg–Si-rich gas. The enrichment of spinel in Si is difficult to explain by the contamination from adjacent phases because if occurred, it would also have changed the contents of other elements. In contrast to forsterite, such enrichment is certainly not due to a nanophase contribution (e.g., SiO_2) but rather due to the amorphous rim contribution. Indeed, although having large error bars, analyses of the amorphous rims (Table 5) of some spinel reveal SiO_2 content up to

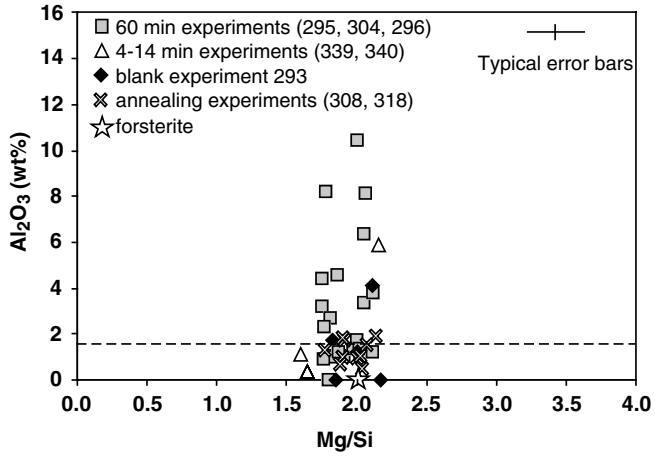

Fig. 9. Concentration of Al_2O_3 (wt%) versus Mg/Si ratio of forsterite from condensation and annealing test experiments of Mg–Si-rich material. Forsterites from blank experiments, 4–14 min experiments (with temperatures from 1045 to 1139 °C), and 60 min experiments (temperatures from 1045 to 1285 °C) show the same enrichment in aluminum independently of their atomic Mg/Si ratio (the star represents stoichiometric forsterite composition). In contrast, forsterites from annealing test experiments (# 308, # 318, Table 2) show no Al enrichment. Because the chemical compositions of forsterite from the ~60 min-experiment are not dependant on the condensation temperature, they were not reported as a function of temperature on the graph. Dotted line gives the analytical TEM detection limit. Numbers in parentheses correspond to the number of the experiment (Table 2).

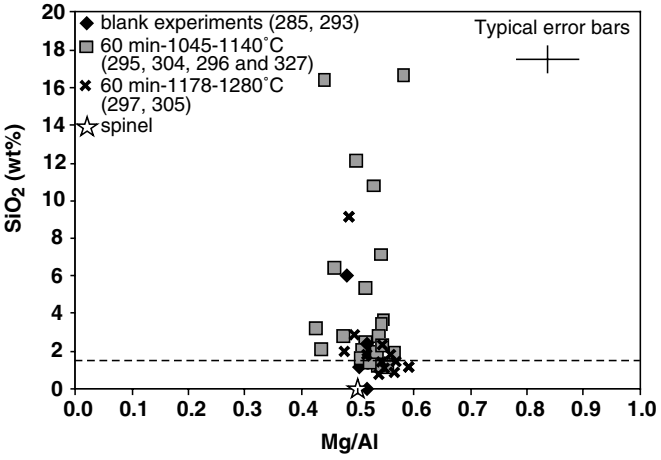

Fig. 10. Concentration of SiO_2 (wt%) versus Mg/Al ratio of spinel from condensation experiments of Mg–Si-rich gas. Spinels from blank experiments are similar to those from ~60 min experiments. Note that high-temperature spinels (>1178 °C) are in average less enriched in SiO_2 than low-temperature spinels (1045–1140 °C). Dotted line gives the analytical TEM detection limit. Numbers in parentheses correspond to the number of the experiment (Table 2).

80%wt. The influence of time on the chemical composition of the spinel is not obvious since only a few spinels were found in the short duration experiments.

3.3.4. Corundum

Corundum is mainly stoichiometric, with no calcium enrichment within detection limits. However, as shown by Fig. 11, it can be slightly enriched in magnesium (up to 8 wt%), independently of the temperature or duration of the condensation experiments. In such cases the composition of corundum lies on the corundum–spinel join. Contribution of the amorphous rims could not account for such compositions. Indeed, analyses of the amorphous rims (Table 5) reveal that they are not homogeneous, and show SiO_2 enrichment, accompanied by either MgO or CaO enrichments. The magnesium enrichment of some corundums could rather be explained by a chemical reaction with the gas during condensation (see Section 5.2.5). Some corundum grains also show large enrichments in silicon (up to 11 wt%), magnesium and calcium (up to 8 and 3 wt%, respectively) that could be related to contamination by adjacent phases during analyses or contribution of the amorphous rim.

Table 5
Mean compositions of condensed crystals of corundum and spinel surrounded by an amorphous rim

		Exp	Gas	Composition (wt%)			
				MgO	Al_2O_3	SiO_2	CaO
Corundum	Crystal	336	Mg–Si	7.60	87.04	4.34	1.01
	Rim	336	Mg–Si	13.47	77.23	7.82	1.48
Spinel	Crystal	327	Mg–Si	27.94	69.26	2.27	0.54
	Rim	327	Mg–Si	3.06	13.72	78.36	4.86
Spinel	Crystal	253	$An_{50}Di_{50}$	30.73	67.11	1.91	0.26
	Rim	253	$An_{50}Di_{50}$	3.46	15.77	72.57	8.21

Mg–Si stands for Mg–Si-rich gas.

3.3.5. Pyroxene

Low-Ca pyroxenes are stoichiometric in terms of cation to oxygen ratios ($4/6 \pm 0.01$). They belong to one of the enstatite polymorphs. They show slight enrichment in CaO and Al_2O_3, with the bulk compositions being consistent with the diopside–enstatite solid-solution (Fig. 12).

Calcic pyroxenes condensed from the Mg–Si-rich gas are also stoichiometric in terms of cation to oxygen ratios ($4/6 \pm 0.01$) and show variable aluminum contents up to 22 wt%, consistent with the diopside–Ca–Tschermak solid-solution (Fig. 13). Although close to the analytical precision, it seems that the calcic pyroxene becomes more aluminous with increasing temperature and run time. Compositions of the calcic pyroxenes from the lower temperature 1045 °C–52 min experiment show large depletions in calcium and lie on the diopside–enstatite join (Fig. 12). The pyroxenes condensed in the Ar ambient gas at low-temperature (e.g., at 1075 °C) are compositionally similar to those condensed in CO_2 ambient gas at low-temperature (<1090 °C). Calcic pyroxenes condensed from the $An_{50}Di_{50}$ gas are, on average, slightly more enriched in aluminum than those condensed from the Mg–Si-rich gas (Fig. 14).

3.3.6. Melilite

Melilite contains various amounts of åkermanite and gehlenite end-members (Fig. 15). It is stoichiometric in

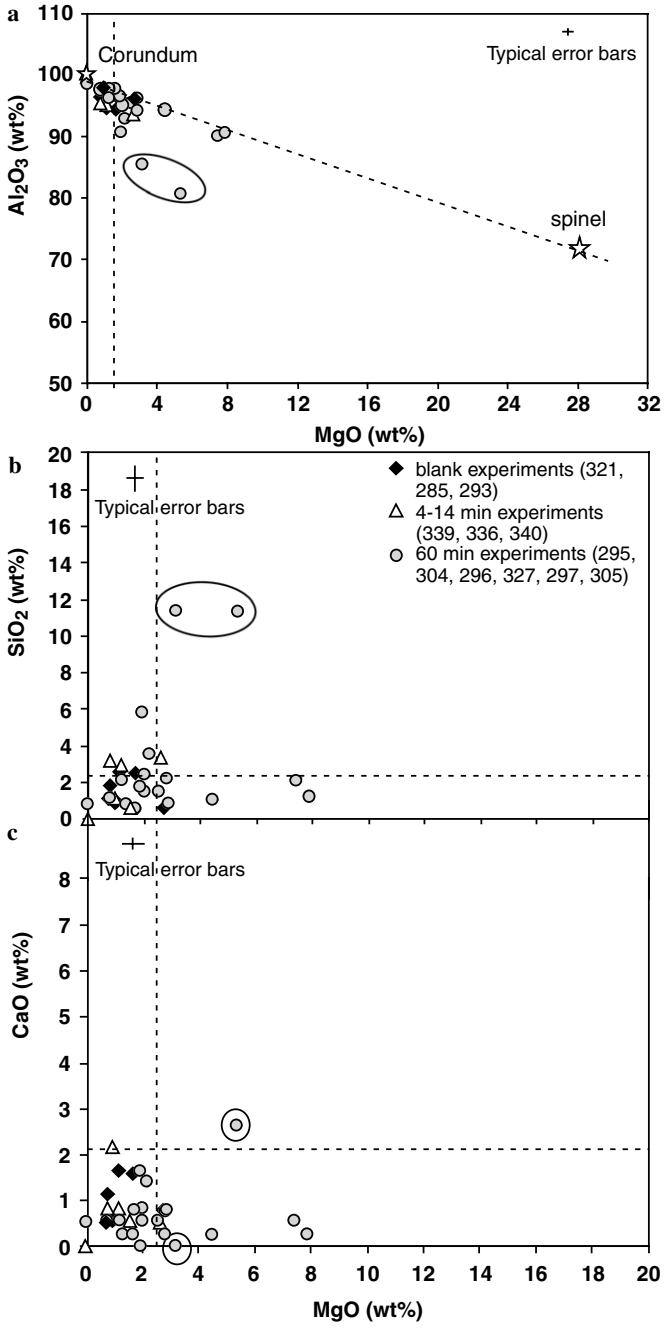

Fig. 11. Concentrations of Al_2O_3, SiO_2 and CaO versus MgO (wt%) in corundum from condensation experiments of Mg–Si-rich gas (graphs a, b, c, respectively). There is no large difference between the corundum from the 4–14 min-experiments, ~60-min experiments and the blank ones. Most corundums are stoichiometric with CaO, SiO_2 and Al_2O_3 within detection limits (dotted lines). However, graph a shows that some corundums enriched in MgO plot toward the spinel end-member. Graphs b and c show that these corundums are, however, not enriched in CaO and SiO_2. The gray dots inside the circle correspond to corundum grains enriched both in MgO, SiO_2 (and CaO for one of them). Because compositions of 60 min-experiment corundum are independent of condensation temperature, they are not reported. Numbers in parentheses correspond to the number of the experiment (Table 2).

terms of cation to oxygen ratios ($5/7 \pm 0.02$). Melilite from the Mg–Si-rich gas-1140 °C–51 min experiment shows variable contents of åkermanite (mean Åk 47). In addition,

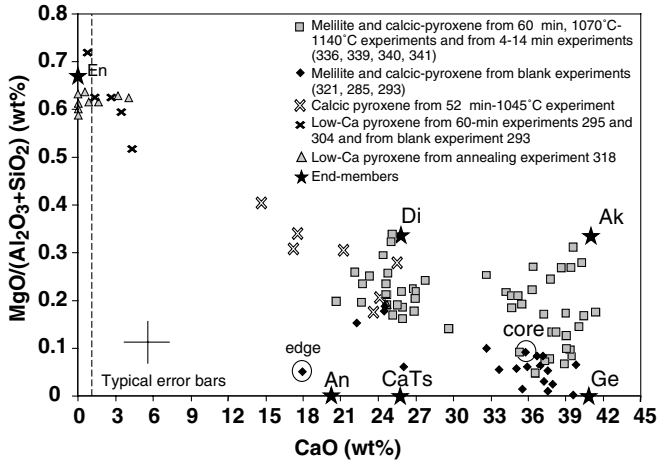

Fig. 12. $MgO/(Al_2O_3 + SiO_2)$ ratio versus CaO (wt%) concentration of pyroxene and melilite from condensation and annealing test experiments of Mg–Si-rich gas. The compositions of pyroxene and melilite lie between the Ca-Tchermak/diopside/enstatite end-members and the åkermanite/gehlenite end-members, respectively. The evolution of the chemical compositions suggests that there might be a continuum between melilite and calcic pyroxene. Encircled black dots indicate the chemical differences between the edge (depleted in calcium) and the core of a single grain (from experiment # 321), suggesting a chemical reaction between the grain and the gas. Note also the difference in chemical composition and evolution between enstatite formed by condensation (experiments # 293, # 295 and # 304, Table 2) and those obtained by annealing (experiment # 318, Table 2). Di, CaTs, En, Åk and Ge stand for diopside, Ca–Tchermak molecule, enstatite, åkermanite and gehlenite, respectively. Dotted line gives the analytical TEM detection limit. Numbers in parentheses correspond to the number of the experiment (Table 2).

melilite is more åkermanitic (Åk 73) in shorter experiments (1140 °C–14, 4 min, CO_2 or Ar ambient gas). Compositions of melilite condensed from the $An_{50}Di_{50}$ gas (1050 °C–61 min or 1145 °C–66 min) are roughly similar to those condensed from the Mg–Si-rich gas (mean Åk 49), except for the lack of the most åkermanitic grains (Fig. 14).

Analyses reveal also that some melilite grains are not chemically homogeneous. For instance, one of them has a melilitic crystalline core and a crystalline rim depleted in Ca and enriched in Si (see Fig. 12).

3.3.7. Rare phases

Rare phases observed in this study include larnite (Ca_2SiO_4) and Ca_3SiO_5 (Tables 2 and 4). Two crystals of larnite found in the Mg–Si-rich gas-1140 °C–51 min experiment # 327 (Table 2) show excess of MgO (up to 3 wt%). Ca_3SiO_5 crystals found in the Mg–Si rich gas-1138 °C–4 min and in the $An_{50}Di_{50}$–1050 °C–61 min experiments (# 340 and # 233, respectively, Table 2) are enriched in aluminum and magnesium (1.5–4 wt%).

4. Condensation tests

In this section, we describe all the experimental tests performed, mainly on the Mg–Si-rich gas composition, in order to prove that the observed crystalline grains were formed by condensation. Since our experiments used la-

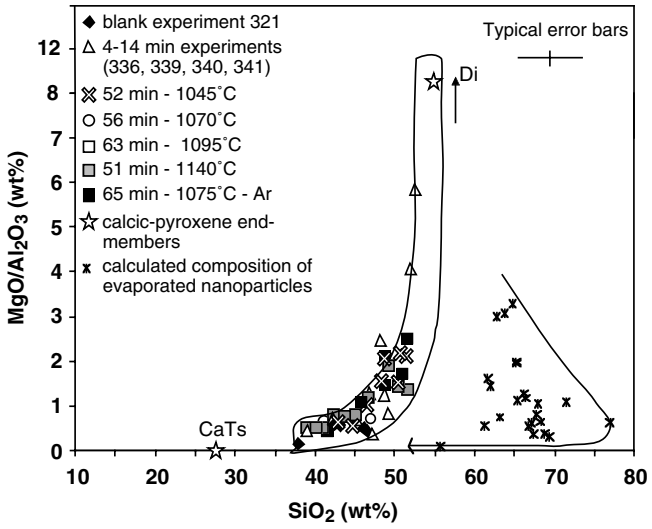

Fig. 13. MgO/Al_2O_3 ratio versus SiO_2 (wt%) of calcic pyroxene from condensation experiments of Mg–Si-rich gas. Calcic pyroxenes from blank and formal experiments are similar. Calcic pyroxenes become less diopsidic with increasing temperature and run time. Calcic pyroxenes condensed in the Ar ambient gas show no difference with those condensed in the CO_2 ambient gas. Calculated compositions of evaporated Mg–Si-rich nanoparticles using our evaporation data were reported on the graph. The large difference in composition between the modelled evaporated particles and the calcic pyroxenes confirms the condensation origin of the latter. On this graph are also reported in outline the range of compositions of natural TiO_2 and FeO poor (<1%wt) calcic pyroxenes from CAIs (sources: diopside from type A CAIs (Grossman, 1975), from CM chondrites, (MacPherson and Davis, 1994), from the fine-grained Yamato 81020 CAI (Itoh et al., 2004), from CAIs from CR chondrites (Aléon et al., 2002), and from spinel-rich inclusions (Kornacki and Wood, 1985)). Numbers in parentheses correspond to the number of the experiment (Table 2).

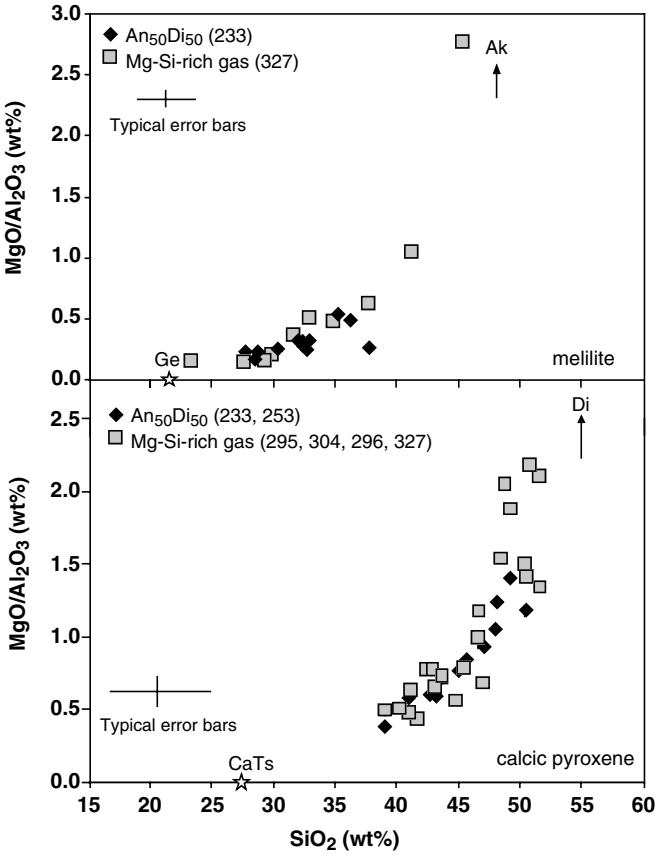

Fig. 14. MgO/Al_2O_3 ratio versus SiO_2 (wt%) concentration of Melilite and calcic pyroxene showing the differences between crystals condensed from $An_{50}Di_{50}$ or Mg–Si-rich gas. Whereas melilites condensed from the $An_{50}Di_{50}$ gas are mostly similar to those condensed from the Mg–Si-rich gas, $An_{50}Di_{50}$ calcic pyroxenes are slightly more enriched in aluminum than the Mg–Si-rich one.

ser-ablation to produce a primary gas and nanoparticle evaporation to produce the secondary gas to be condensed, it is important to demonstrate that the ablation droplets and the nanoparticles could neither result in the formation of the observed crystalline phases on the Pt-grid nor influence the condensation process.

4.1. Crystallization of laser-ablation droplets

It is necessary to ensure that the crystalline phases observed in our experiments have not been formed by the crystallization of partially evaporated laser-ablation droplets. The crystallization of large laser-ablation droplets could result in the formation of phases such as anorthite and diopside in the $An_{50}Di_{50}$ experiments, or to the crystallization of forsterite and enstatite in the Mg–Si-rich experiments. If these droplets partially evaporate (e.g., loss of magnesium in Fig. 7), they may form more refractory phases. However, the crystallization of such droplets would produce either single crystals embedded in a certain amount of melt or several crystals of similar or different chemical compositions whose bulk composition accounts for that of the melt. None of these features is observed in our experiments. For all run times and condensation temperatures, laser-ablation droplets found on Pt-grids are not crystalline. They are quenched amorphous droplets deposited on the Pt grid where the temperature was too low (<1250 °C) to allow their crystallization in 1 h or less.

4.2. Annealing of the nanoparticles

Two types of test experiments were performed to show that the observed condensates could not be formed by the aggregation of annealed nanoparticles in the gas or on the Pt-grid. The first experiment was a classical annealing experiment with nanoparticles deposited on a cold grid and subsequently reheated. The second experiment aimed at testing the annealing occurring during collection on a grid in thermal equilibrium with a hot background gas.

In the first test experiment (# 308, Table 2), nanoparticles condensed from a Mg–Si-rich gas at 25 °C, $\sim 4 \times 10^{-3}$ bar of CO_2 were collected during 52 min on a vertical Pt-grid inside a cold furnace. Then, in the same run ($\sim 4 \times 10^{-3}$ bar of CO_2) these nanoparticles were heated at 1070 °C during 62 min, typical conditions of a condensation experiment. TEM observations of the products showed that annealing of Mg–Si-rich nanoparticles results

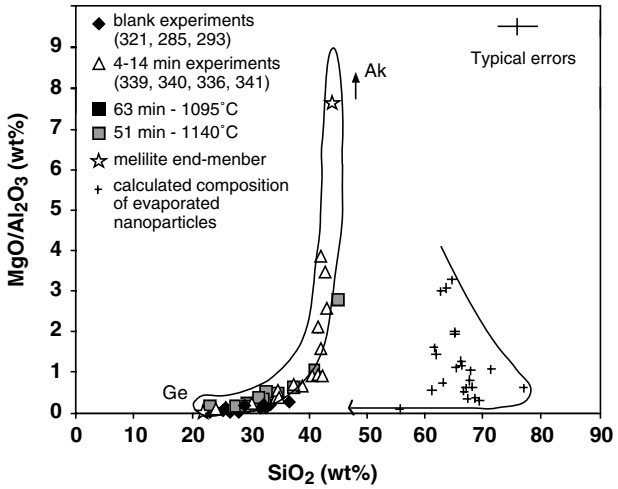

Fig. 15. MgO/Al_2O_3 ratio versus SiO_2 (wt%) of melilites from condensation experiments of Mg–Si-rich gas showing that all condensed melilite lie on the åkermanite–gehlenite solid-solution. Melilites from short-time experiments (in CO_2 or Ar ambient gas) are more åkermanitic than those from ~60 min-experiments. Melilites from blank experiments are more gehlenitic than other ones. Calculated compositions of evaporated Mg–Si-rich nanoparticles using our evaporation data were reported on the graph. Again, condensed melilites do not follow the evaporation trend. On this graph are also reported in outline the range of compositions of natural melilites from CAIs (sources: melilite from fluffy type A CAIs (Christophe Michel-Lévy, 1981), from type B in CV Vigarano chondrite (Davis et al., 1991), from compact type A (Podosek et al., 1991), from type B in CV Allende chondrite (Bischoff and Palme, 1987), from CAIs from CR chondrites (Aléon et al., 2002), and from the fine-grained Yamato 81020 CAI (Itoh et al., 2004)).

in the formation of a continuous thick film (~300 nm) of crystalline olivines (see Fig. 16d). The presence of a small amount of glass is also expected to account for the initial nanoparticle composition. The olivines, whose chemical composition are reported in Fig. 9 and Table 4, are stoichiometric, with no calcium and aluminum within detection limits, in contrast to the olivines of condensation origin (e.g., Fig. 9 or Table 4, # 304). Note that duration of annealing was comparable to those reported in other studies (e.g., Fabian et al., 2000; Rietmeijer et al., 2002).

In the second test experiment (# 318, Table 2), nanoparticles condensed from a Mg–Si-rich gas between 300 and 500 °C ($\sim 4 \times 10^{-3}$ bar of CO_2) were collected on a vertical Pt-grid at the bottom of the furnace (just at the bottom of the evaporation zone), at grid temperature of 1040 °C (in zone 3) during 67 min. TEM observations of the Pt-grid revealed the presence of crystals of enstatite and forsterite which covered most of the grid (Fig. 16c). Again, the olivines are stoichiometric, with no calcium and aluminum in contrast to the condensed olivines (Fig. 9). The enstatite shows very slight enrichment in Ca and Al but does not lie on the enstatite–diopside join (Fig. 12).

Thus, the annealing of Mg–Si-rich nanoparticles results in products with compositions expected from the crystallization of Mg–Si-rich material. It does not yield phases with compositions similar to our condensates. In addition, the texture, size and morphology of the crystals formed by annealing of the nanoparticles are different (e.g., compare Fig. 16c, d and 8 or 18) from those condensed from a gas. Notice that although the observation of enstatite in test experiment # 318 may be indicative of slight evaporation of the nanoparticles at the bottom of the furnace, this test experiment shows that the evaporation of the nanoparticles before their entrance in the furnace was negligible.

4.3. Annealing of partially evaporated nanoparticles

In order to test whether the crystalline phases observed in our experiments can be formed by the annealing of partially evaporated Mg–Si rich nanoparticles, we calculated compositions of such particles based on the evaporation data from the laser-ablation droplets (e.g., Fig. 7).

Compositions of laser ablation droplets recovered (1) in calibration experiments before their entrance in the furnace and (2) on the Pt-grids after 1-h high-temperature condensation experiments were determined by EDX-TEM. Compositions of the laser ablation droplets recovered on the Pt-grid were normalized to the mean composition of those captured before the entrance in the furnace in order to define enrichment/depletion coefficients due to evaporation. The depletion coefficient of Mg was taken as a proxy for the amount of evaporation. Starting from the unfractionated composition, theoretical compositions of evaporated nanoparticles were calculated using these coefficients.

It was found that evaporation of Mg–Si-rich nanoparticles might result in the formation of particles compositionally similar to anorthite, gehlenite or corundum with increasing rate of evaporation (Fig. 12). However, the chemical variations shown by melilite and pyroxene (Figs. 13 and 15) observed in the formal experiments cannot be reproduced by this model. In addition, clusters of "corundum" residues from nanoparticle evaporation were observed in the calibration experiment # 343 (Table 2), where evaporation temperature was not high enough to completely vaporize the nanoparticles. Although crystalline, they have, however, a texture completely different from that of the condensed euhedral corundums (Fig. 16a and b).

Thus, with the possible exception of anorthite, the observed crystalline phases are unlikely to result from the annealing of partially evaporated nanoparticles.

4.4. Blank experiments

To ensure that (1) the crystalline phases formed in our condensation experiments did not result from secondary reactions between the gas and partially evaporated nanoparticles, and that (2) the possible pre-existing silicate or oxide nuclei in the formal experiments did not influence the condensation process, we have performed special experiments, hereafter referred to as blank experiments (Fig. 17). They were carried out using Pt-furnaces lined with porous alumina tubes from previous formal experiments, i.e. saturated with evaporated Mg–Si-rich gas and partially covered

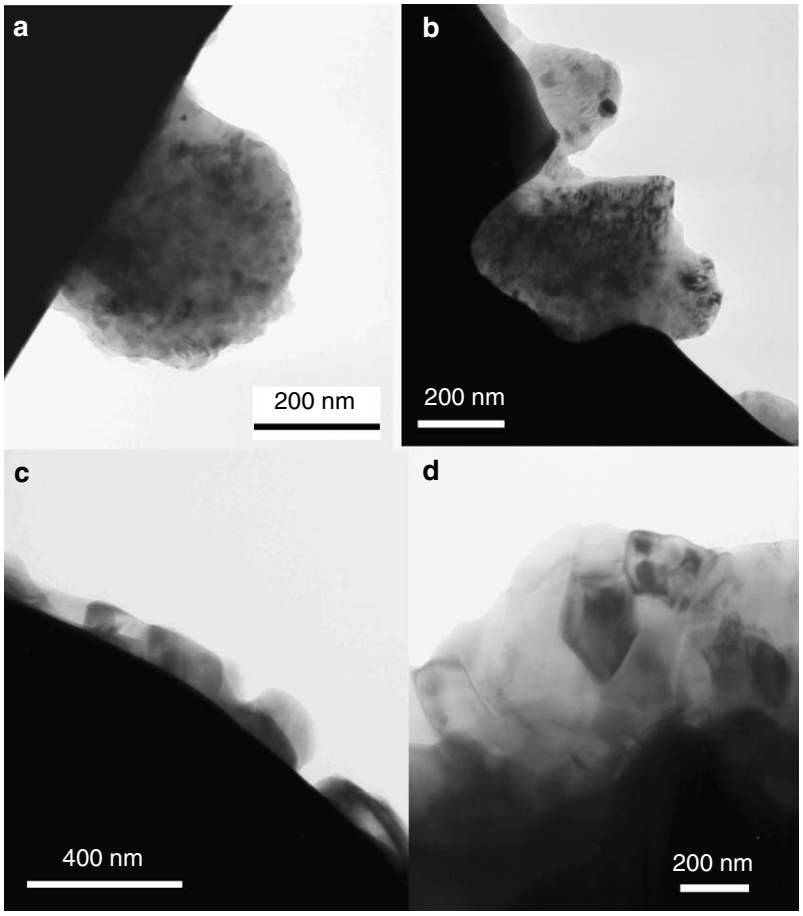

Fig. 16. Bright field transmission electron micrographs of products of the calibration and annealing test experiments. (a and b) Crystallized aluminous products of calibration experiments # 343 (evaporation temperature of 1015 °C). (c) Forsterite and enstatite from experiment # 318 of annealing of Mg–Si-rich nanoparticles (1040 °C, 67 min, $\sim 4 \times 10^{-3}$ bar of CO_2, bottom of the furnace). (d) Forsterite crystals from experiment # 308 of annealing (1070 °C, 62 min, $\sim 4 \times 10^{-3}$ bar of CO_2) of Mg–Si-rich nanoparticles condensed at 25 °C. Note that the crystals produced during the annealing experiments cover the entire platinum TEM grid.

with laser ablation droplets. Before performing blank experiments, the alumina tubes were partially cleaned using the same HF–HCl chemical treatment as for the Pt-furnace. Pt-grids were then held in these furnaces heated up to 1077, 1125 and 1250 °C (T_c) at 10^{-3} bar of CO_2 during 278, 143 and 300 min, respectively (experiments # 321, 293 and 285, respectively, Table 2).

Although the gas evaporating from the alumina rods was free of any nanoparticles and laser ablation droplets, these blank experiments yielded condensation of crystals on the Pt-grid with similar textures and structures to those condensed during formal experiments using laser ablation (Fig. 18). Crystals ranging from 50 to 300 nm in size were euhedral to spherical (Fig. 18c and e), with few crystallographic defects at the TEM scale. Some crystals have also an amorphous rim on their surface (Fig. 18c). They have various textures: single crystals (Fig. 18a–c), aggregates of crystals of similar composition (300 nm) (Fig. 18f), chains of euhedral crystals (>2 μm long) of different or similar mineralogy (Fig. 18d). In addition, spinel and corundum were also observed as plates stacked together (Fig. 18e).

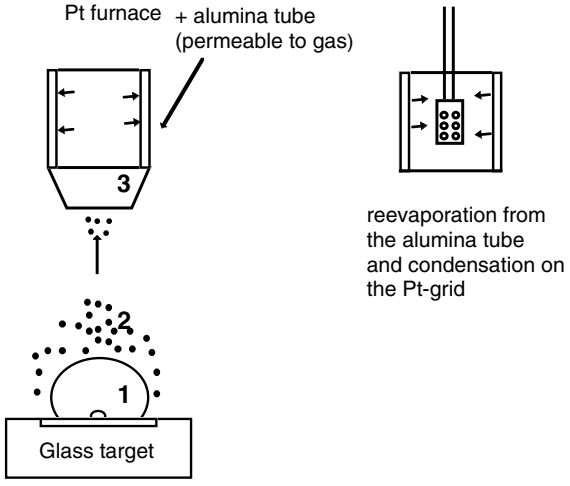

Fig. 17. Schematic drawing of the blank experiments.

As reported in Table 2, all the mineralogical phases observed in the formal experiments were also found to condense in these blank experiments. In addition, based on chemical composition, one crystal of hibonite was identi-

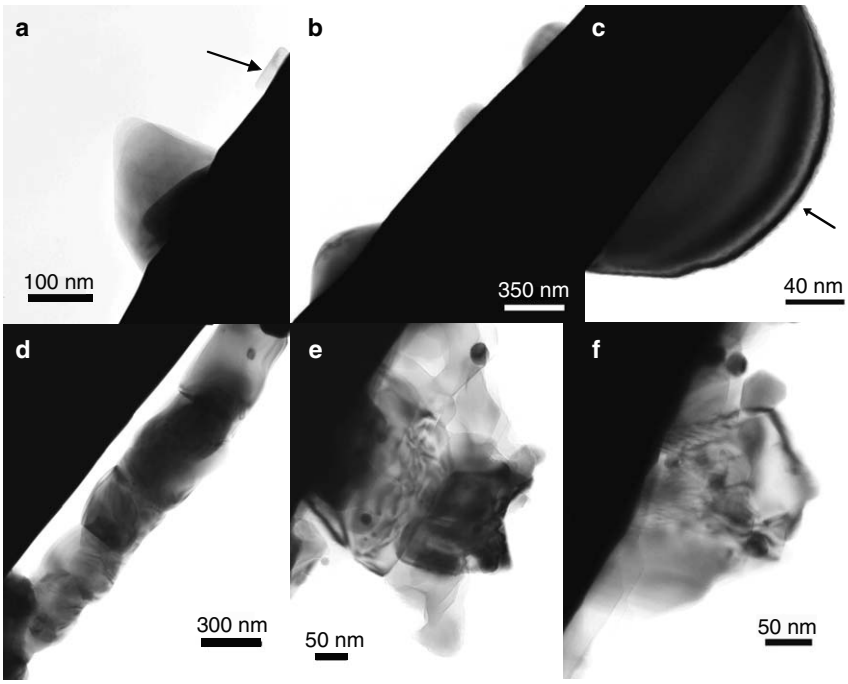

Fig. 18. Bright field transmission electron micrographs of high-temperature condensates from blank experiments ($\sim 4 \times 10^{-3}$ bar total pressure). (a) Crystal of anorthite, the arrow indicates the presence of an euhedral crystal ($T_c = 925$–1077 °C, 278 min; Table 2, # 321). (b) Micrograph showing the usual distribution of the crystals on the platinum TEM grid ($T_c = 960$–1125 °C, 143 min; Table 2, # 293). Crystal at the bottom of the micrograph is an anorthite. (c) Spherical crystal of anorthite bordered by an amorphous rim indicated by an arrow ($T_c = 850$–1250 °C, 300 min; Table 2, # 285). (d) Chain of euhedral crystals of forsterite and anorthite ($T_c = 960$–1125 °C, 143 min; Table 2, # 293). (e) Corundum crystals stacked together ($T_c = 960$–1125 °C, 143 min; Table 2, # 293) showing features looking like platelets. (f) Aggregate of corundum crystals ($T_c = 960$–1125 °C, 143 min; Table 2, # 293).

fied in the 925–1077 °C (278 min) experiment # 321 (Table 4). Because neither the temperature was constant, nor the chemical composition was well controlled in these experiments, the variations of the mineralogy with temperature are more difficult to understand. Nevertheless, the most refractory minerals (e.g., spinel, corundum) were also found in the highest temperature experiment.

Chemical compositions of minerals found in these experiments are reported in Figs. 9–15. Forsterite, anorthite, corundum and spinel do not show any differences from those condensed in formal experiments (Fig. 9–11). Melilites are more gehlenitic (mean Åk 20) (Fig. 15). Calcic pyroxenes are similar (Fig. 13) to those condensed in formal experiments except for one grain, which is very Al-rich (31 wt% of Al_2O_3).

The test experiments show unequivocally that the observed phases in the formal experiments are condensed crystals. Our experimental technique of high-temperature condensation of a multi-elemental gas (e.g., use of a laser or of nanoparticle evaporation) does not influence the nature of the condensation products nor the condensation process.

5. Discussion

5.1. Unresolved questions

Since condensation process is largely involved in the cycle of dust in the galaxy, from its formation in evolved stars such as Asymptotic Giant Branch stars, red giants or supernovae to its formation in the protoplanetary accretion disks, numerous studies, mostly theoretical, were focused on understanding dust condensation. Condensation can be divided into two processes, which are closely related to each other, (1) nucleation, i.e. the mechanism by which a stable nucleus is produced in the gas and (2) growth of the particle in the gas. Nucleation can be considered either as a statistical phenomenon of an ensemble of particles (classical thermodynamics) or as a consequence of a specific chain of networked chemical reactions with specified rates. Because of the very large number of chemical reactions involved in the formation of complex silicates, nucleation has usually been modelled using modified classical theories of nucleation (e.g., Blander and Katz, 1967; Salpeter, 1977; Draine, 1979; Cameron and Fegley, 1982; Gail and Sedlmayr, 1986, 1987). However, because of the lack of experimental data (e.g., surface energy), nucleation in protostellar or circumstellar environments (Sedlmayr and Krüger, 1997; Tielens et al., 1998) is still poorly understood. Processes of particle growth are particularly studied for stellar envelopes where the rapid expansion of the dust shell limits the timescale for equilibrium of the grains with the gas and their growth (e.g., Dominik et al., 1993; Gail and Sedlmayr, 1999).

Most of the work has focused on the chemical composition of the dust condensed at equilibrium from a solar gas or from a gas with elements in solar proportion except for carbon (variable C/O ratios) (e.g., Lord, 1965; Gilman,

1969; Grossman, 1972; Larimer and Bartholomay, 1979; Sharp and Wasserburg, 1995; Lodders and Fegley, 1997; Petaev and Wood, 1998; Ebel, 2000). Thus, a "condensation sequence" of minerals forming at equilibrium from a cooling solar gas is widely used to explain the chemical properties of planets (Barshay and Lewis, 1976), meteorites (Larimer and Anders, 1970; Palme, 2000), their components (e.g., CAIs, Grossman, 1975), interstellar dust (e.g., Bernatowicz and Cowsik, 1997), and ultimately the conditions prevailing in their environments of formation. However, although thermodynamic models take into account all possible chemical reactions among the gaseous and condensed species included in their thermodynamic databases, they do not predict the chemical paths for individual reactions (e.g., transition states? energy barriers?), nor the rates at which they proceed. The influence of energy barriers, for instance, may significantly alter the predictions of these models (e.g., Fegley and Prinn, 1989; Fegley, 2000).

5.2. Experimental contribution

5.2.1. Nucleation and crystal growth

5.2.1.1. Nucleation in the gas. Both the number and the size of the crystals increase with experiments duration which indicates that crystal growth did not inhibit nucleation of new crystals. This reflects the simultaneous occurrence of two processes in the furnace during the course of an experiment: the nucleation of grains from the gas entering continuously the furnace and the growth of the already condensed grains in thermal equilibrium conditions (as the grains on the Pt-grid have the same temperature as the gas). The morphology of the crystals growing on the Pt-grid (Fig. 8) suggests that condensation occurred largely on the Pt-grid, without an epitaxial relation between the substrate and the condensed crystals (Volmer–Weber growth mode, Zhang and Lagally, 1997). However, the occurrence of chains of euhedral crystals of different or similar mineralogy (e.g., Fig. 8h) suggests that these crystals directly formed in the gas by condensation and stacked together in the gas to form a chain. Their nucleation in the gas might have been induced by the presence of remaining Al-rich nuclei from the evaporation of the nanoparticles or by the presence of some small laser-ablation droplets in the furnace. However, the occurrence of chain-like crystals in the blank experiments, i.e. in the total absence of silicate or oxide nuclei, supports their formation by direct nucleation in the gas.

5.2.1.2. Morphology of the crystals. Most crystal morphologies observed in our experiments (melilite, anorthite, forsterite, enstatite and Al-diopside) are not specific to condensation (e.g., euhedral crystals). However, rounded crystals are not commonly observed and may be characteristic of grain growth from a gas. Spinel and corundum crystals were often found as platelets stacked together. The corundum morphology could be explained by (1) the affinity of corundum to form platelets (Givargizov, 1987) and/or (2) the growth of corundum at supersaturation which favors the kinetically controlled growth of platelets. Spinel platelets may be attributed to their formation from corundum platelets (see Section 5.2.4). Finally, spinel whiskers are commonly observed associated to spinel platelets (Givargizov, 1987). Whisker and platelet morphologies are typical of grain growth from a gas. Such habits of olivine and pyroxene have already been observed in interplanetary dust particles (e.g., Bradley et al., 1983) and in meteorites (e.g., Weisberg et al., 1997).

5.2.2. Crystallinity of the condensed phases

Because of the difficulty in performing equilibrium high-temperature condensation experiments, previous experimental evidence concerning the degree of crystallinity of gas-to-solid condensates was not unequivocal (Nagahara et al., 1988; Nuth et al., 2000 and references therein). In their condensation experiments, Nagahara et al. (1988) succeeded in condensing crystalline olivine, pyroxene, a silica mineral and metallic iron from 1200 to 500 °C in H_2 at 10^{-9} bar from a Mg–Fe–Si–O–H gas produced by vaporization of olivine. Based on the euhedral shape of the condensed olivine, they suggested that the condensates were crystalline as soon as they condense. However, as their experiments were long (several tens of hours), the role of annealing processes on the crystallinity of their condensates was difficult to quantify. Other experiments were performed in non-equilibrium and low temperature conditions and thus, do not provide answers to the questions of the degree of crystallinity of the high-temperature equilibrium condensates (e.g., Arrhenius and Alfvén, 1971; Day and Donn, 1978; Stephens and Kothari, 1978; Nuth et al., 2000). For instance, Nuth et al. (2000) have performed non-equilibrium condensation of e.g., Mg–SiO–H_2–O_2 or Al–SiO–H_2–O_2 vapors at ~0.1 bar on short timescales and found that in the temperature range of 227–827 °C, only amorphous material are condensed, with compositions interpreted to be imposed by inferred metastable "eutectics" of the corresponding phase diagrams (e.g., Rietmeijer et al., 1999).

In our experiments, phases were crystalline (i.e. either totally crystalline or with a 3–10 nm amorphous rim) under all conditions including the shortest run times of 4 min (e.g., Fig. 8b and f). Several possibilities can be considered: (1) annealing of liquid droplet condensates of non-stoichiometric composition, (2) annealing of liquid droplet condensates of stoichiometric mineral composition and (3) direct condensation of crystals.

The annealing of liquid droplet condensates of non-stoichiometric composition is likely to yield the formation of several crystals of different composition, which has not been observed (see also Section 4.1). In addition, in the case of formation of single crystals, the amorphous rims cannot be considered as residues from the crystallization of such amorphous droplets because their very small volume relative to that of the crystals would imply that the initial composition of the droplet was very close to that of the final

crystal. Note also that the characteristics of the rims (e.g., thickness, occurrence) are independent on the experiment durations contrary to what is expected in the case of annealing.

The annealing of liquid droplet condensates of stoichiometric mineral composition is also highly unlikely because crystalline condensates (e.g., enstatite, forsterite, Al-diopside or melilite) were also recovered in the top, low-temperature part (800–900 °C) of the furnace in additional experiments (~1 h). These condensates have spent less than a few seconds in the furnace. They are thus likely to be already crystalline when they reached the Pt-grid since these temperatures are too low for annealing on such a timescale (e.g., ~800 °C, Fabian et al., 2000).

Our experiments indicate that at high-temperature (and low pressure), solids condense directly as crystals. The occurrence of amorphous rims suggests that mechanisms of crystal growth may involve a boundary layer between gas and crystal, facilitating the accommodation of chemical elements and the ordered growth of the crystal. The rims show chemical compositions supporting this mechanism since they are usually enriched in the elements which do not enter in large amount in the host crystals (e.g., Si-rich rim for spinel, see Table 5). Under our conditions, both supercooling needed to initiate nucleation (e.g., to overcome surface energy barriers) and kinetics of chemical and surface reactions (e.g., rate of atoms attachment or diffusion of atoms at the surface of the grains) did not result in the formation of amorphous material during high-temperature condensation process (e.g., Salpeter, 1977; Cameron and Fegley, 1982). Our results do not support models (Blander and Katz, 1967) of preferential condensation of metastable liquid droplets rather than crystalline phases.

5.2.3. Attainment of a steady state

Experiments at 4, 14 and 60 min (CO_2 ambient gas, Mg–Si-rich gas) show that most mineralogical changes occur in the first 10–20 min (~4×10^{-3} bar, ~1140 °C). Reactions involved in the formation of the different phases (e.g., nucleation, chemical reaction with the gas phase and diffusion in the grains) are thus rapid enough to attain a steady state in less than 1 h at ~4×10^{-3} bar and 1140 °C. We infer that a steady state was also attained in ~1 h for all temperatures studied here.

This observation reveals that chemical reactions involved in the grain growth are rapid enough for the grains to reach chemical equilibrium with the gas in less than 1 h. Thus, despite the occurrence of nucleation during the entire experiment, once a steady state is reached, the crystals that are in chemical equilibrium with the gas dominate the condensate. In contrast to earlier far-from-equilibrium experiments (e.g., Day and Donn, 1978; Nuth et al., 2000), our experiments can thus be considered as the first successful near-equilibrium laboratory condensation. Therefore, it appears that under astrophysical conditions similar to those of our experiments chemical equilibrium should be attained on the timescales of ~1 h or less.

5.2.4. Chemical fractionation of the gas

Experimental condensation of Mg–Si-rich gas results in the formation of minerals. Our results therefore confirm that condensation of amorphous phases with stochastic composition is not favored. Being 50 nm to 4 μm in size, most of our condensates may not be considered as nanoparticles and their properties can be compared with those expected for macroscopic samples. The experimentally condensed minerals are among those thermodynamically predicted to form at high-temperature in a closed-system at equilibrium (e.g., Wood and Hashimotom, 1993; Ebel and Grossman, 2000). Furthermore, our experiments show that high-temperature condensation of a multi-elemental refractory gas at ~4×10^{-3} bar results in the formation of crystals whose chemical compositions and proportions vary with gas composition ($An_{50}Di_{50}$ or Mg–Si-rich gas), temperature (1045–1285 °C) and duration of condensation (4–66 min). Thus, the condensation process results in a chemical fractionation of the gas varying with these parameters.

The mineralogical evolution of the condensates with temperature is qualitatively consistent with that predicted by thermodynamic calculations (e.g., Petaev and Wood, 1998; Ebel and Grossman, 2000), with less refractory minerals forming at low temperature in ~1-h steady-state experiments (Fig. 19). Therefore, our results define an experimental condensation sequence as a function of temperature.

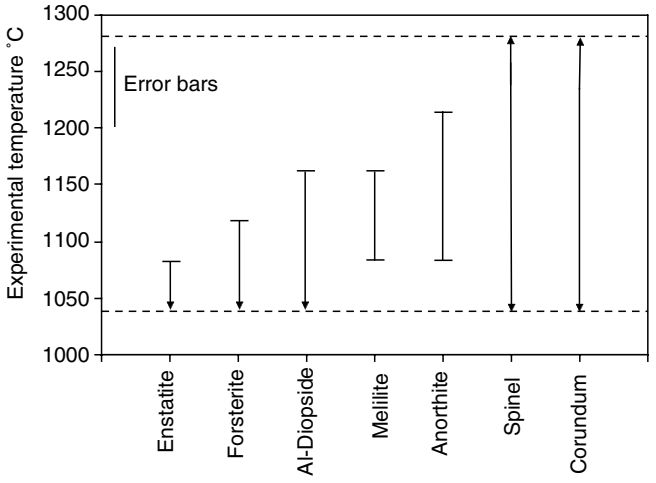

Fig. 19. Experimental range of condensation temperatures of phases formed from the Mg–Si-rich gas at a total pressure of ~4×10^{-3} bar (CO_2). Experimental data are given for run time of ~60 min. Dotted lines limit the experimental range of condensation temperatures. Experimental temperatures of appearance of the phases have been extrapolated from their experimental occurrences listed in Table 3 (except for the 1178 °C-forsterite, experiment # 297, Table 2). Stability fields are represented by straight lines. Horizontal lines on the straight lines indicate that the temperature of disappearance of a phase has been determined whereas arrows indicate that either the temperature of disappearance is below 1045 °C, or that the temperature of appearance was not determined. Error bars are ±35 °C.

5.2.5. Influence of kinetics on the condensation process

Our experiments provide two ways to study the effects of kinetics on the condensation process. First, the changes of mineralogical and chemical composition of the condensates as a function of time may give information about the reactions of the grains with the gas, which control the formation and disappearance of phases. Second, as the experimental condensation process takes place in a system with a constant supply of gas in the condensation zone, the mineralogical assemblages observed at steady state may reveal the phases whose formation is kinetically favored. On the contrary, in a closed system at equilibrium, early formed kinetically favored phases may disappear as system reaches an equilibrium state.

Despite the observation of an experimental condensation sequence as a function of temperature in the Mg–Si-rich system, the systematic presence of corundum at all temperatures (1045–1280 °C) points to a fast kinetics of nucleation of corundum (Fig. 19). The presence of corundum in all blank experiments indicates that it forms rapidly even without pre-existing nuclei that could be present in the formal experiments (Al-rich nuclei or small laser ablation droplets). The absence of hibonite or other Al–Ca-rich refractory phases at high temperature in almost all the experiments suggests that their nucleation was not kinetically favored compared to that of the corundum. The absence of corundum, in the $An_{50}Di_{50}$ system suggests, however, that kinetic effects are sensitive to gas composition. For instance, in this system, reequilibration of the corundum with the gas phase could be more rapid than its nucleation or some phases may nucleate more easily than corundum. Note that the rapid kinetics of formation of the corundum in the Mg–Si experiments is certainly not related to a buffering of the Al partial pressure by the alumina lining of the furnace since, for e.g., the aluminum content of pyroxene and melilite varies with condensation temperatures whereas corundum is present at all temperatures.

The presence of corundum with high Mg content (Fig. 11), the absence of spinel in short experiments and the similarity of crystal morphology between corundum and spinel all suggest that spinel is formed rapidly by a back-reaction of the corundum with the gas phase. In addition, its occurrence over the whole experimental range of temperatures (1045–1280 °C) indicates its slow rate of reequilibration with the gas phase. As evaporation of laser ablation droplets will not change the composition of the gas in magnesium by more than 10% (see Section 2.3), its influence on the kinetics of spinel formation can be considered negligible. Thus, in the Mg–Si-rich system, the formation of spinel is kinetically favored.

The occurrence of melilite in the short experiments also suggests a fast kinetics of condensation for melilite. However, it is premature to draw conclusions about its nucleation rate because melilite could also form by reaction of a primary phase with the gas. Nevertheless, the occurrence of Mg-rich melilite in short experiments points out that either nucleation of åkermanitic melilite is kinetically favored or that the primary phase was Mg-rich. The chemical compositions of pyroxene and melilite along with the chemical zoning in melilite (Fig. 12) suggest that pyroxenes could be the products of reaction between melilite and the gaseous phase, but other modes of formation such as direct condensation of pyroxenes from the gas cannot be excluded. Forsterite shows aluminum contamination, probably due to the presence of Al_2O_3 impurities in the crystals, which indicates that olivine could have nucleated on preexisting corundum. The presence of Al-rich forsterite in the blank experiments indicates that these corundum nuclei may not be the nanometer-sized Al-rich evaporation residues possibly present in the formal experiments but rather suggests the nucleation of forsterite on previously condensed corundum.

Our observations show that kinetic parameters can play a key role on the mineralogical assemblages and chemical compositions of the crystals formed by condensation. As the observed kinetics of grain formation highly depends on grain physical properties, the kinetics observations reported in these experiments may help to better understand the mineralogy of the grains condensing from a solar nebula gas, even if some experimental conditions (e.g., metastablity of the gas, composition of the gas) are different from the conditions of condensation in the solar nebula.

5.3. Application to the formation of circumstellar and nebular dust

5.3.1. Nebular condensates

The Ca–Al-rich refractory inclusions (CAIs) from the primitive chondritic meteorites provide valuable information about the early nebula because they are the oldest objects of our solar system (Gray et al., 1973; Amelin et al., 2002). Furthermore, as their mineralogy is close to what is predicted at high-temperature in a theoretical condensation sequence (Christophe Michel-Lévy, 1968; Grossman, 1975; MacPherson, 2004), they may represent the first material condensed from the hot nebular gas. However, studies have shown that some, such as type B and C CAIs (Stolper, 1982; Wark and Lovering, 1982; Beckett and Grossman, 1988), or the compact type A CAIs (e.g., Simon et al., 1999) have probably crystallized from molten objects and could have also underwent a complex series of events including evaporation (Grossman et al., 2000, 2002; Richter et al., 2002) or partial melting (MacPherson and Davis, 1993). The complex history of other CAIs, such as fluffly type A inclusions (e.g., MacPherson and Grossman, 1984), spinel rich objects (MacPherson et al., 1983; Fegley and Post, 1985; Kornacki and Wood, 1985; McGuire and Hashimoto, 1989; MacPherson and Davis, 1994; Lin and Kimura, 2003; Krot et al., 2004a) or amoeboid olivine aggregates (Grossman and Steele, 1976; Komatsu et al., 2001; Krot et al., 2004b; Weisberg et al., 2004) is still not well understood (MacPherson et al., 1988; MacPherson, 2004). Their texture (e.g., fluffy aggregates of concentric

objects for the spinel-rich inclusions) and irregular shape (e.g., amoeboid olivine aggregates) argue against crystallization from a liquid, with some inclusions such as most fine-grained spinel rich objects, showing a group II rare earth element pattern, interpreted as a condensation signature (Boynton, 1975; Kornacki and Wood, 1985; Sylvester et al., 1993). Numerous authors have therefore suggested that they may have formed by aggregation of high-temperature condensates. However, evaluation of the effect of kinetics on the condensation process, and knowledge of the structure and texture of condensates are missing in establishing their origin by direct condensation. In the absence of experimental evidence, different other origins for this type of refractory inclusions have been proposed, which require very specific nebula conditions. For instance, in a study on nucleation of grains from the solar gas, it has been proposed that grains could form in the nebula by growth of amorphous chemical heterogeneous matter on corundum nuclei and experience annealing at high temperature that would result in a complex structure (e.g., Cameron and Fegley, 1982).

Our high-temperature experimental condensates from the Mg–Si-rich gas reproduce the crystallinity of CAIs minerals. In addition, although our crystals have not condensed from a true solar gas (e.g., H_2-bearing, oxygen fugacity, titanium–iron-bearing composition), their compositions reproduce fairly well those of most CAI minerals (Figs. 13 and 15). Note that whereas hibonite, which is observed in CAIs, has not been observed in our experiments, corundum, which is not common in CAIs, is largely observed in our experiments. These differences may be attributed to the experimental conditions of condensation different from that of the solar nebula ($T_c < 1300$ °C, continuous flow of gas entering the furnace that favors continuous nucleation). Both the crystallinity and the chemical composition of our experimental condensates support models of CAIs formation by condensation from a hot solar gas in a relatively short period of time (<1 day, $P_T = \sim 10^{-3}$ bar). Besides the direct formation of grains in the gas, nucleation and grain growth occur mainly on a solid medium (Pt-grid and possibly Al-rich residues) in our experiments. Similarly, CAIs minerals may have nucleated on seed nuclei that should be present in nebular disks (e.g., refractory metals, nanometer-sized refractory presolar dust, e.g., Cameron and Fegley, 1982).

In addition, as our experiments show that kinetics effects can control the mineralogy of the condensates, our experiments suggest that the formation of CAIs with peculiar mineralogy and texture that contradicts equilibrium condensation calculations may be better understood if kinetic effects are taking into account (e.g., inversion melilite/spinel).

Finally, this study also suggests that igneous CAIs have not crystallized from metastable liquid droplets (Blander and Fuchs, 1975) condensed from the gas. Several studies have suggested that they either formed from stable liquid condensates under high dust/gas ratio or high total pressure (e.g., Wood and Hashimotom, 1993; Yoneda and Grossman, 1995), or from molten precursors (e.g., Stolper, 1982).

5.3.2. Stellar condensates

Most of the interstellar refractory dust controlling the chemistry and physics of the interstellar medium (ISM) is formed in the outflows from evolved stars (Gehrz, 1989). Infrared (IR) observations have shown that such dust is dominated by Mg-rich amorphous silicates (Woolf and Ney, 1969; Day and Donn, 1978; Tielens et al., 1998), with few crystalline silicates (forsterite, enstatite and possibly diopside and melilite) (e.g., Waters et al., 1996; Demyk et al., 2000; Molster et al., 1999, 2002) and oxides (corundum, spinel and FeO) (e.g., Molster et al., 1999; Fabian et al., 2001; Kemper et al., 2002, respectively). In addition, the findings of presolar grains in primitive chondrites, whose anomalous isotopic compositions point to their formation in stellar envelopes, have shown that crystalline corundum, spinel, hibonite and silicates can be formed in such environments (Nittler et al., 1994, 1997; Huss et al., 1994; Choi et al., 1998, 1999; Stroud et al., 2002; Messenger et al., 2003; Nagashima et al., 2004). However, because of the lack of experimental data, the conditions of formation of interstellar refractory dust are still poorly constrained.

Although astronomical observations predict low pressure in stellar atmospheres (10^{-9} to 10^{-7} bar), nucleation models (Salpeter, 1977) and studies of presolar grains (Bernatowicz and Cowsik, 1997; Bernatowicz et al., 1996) suggest that pressures above 10^{-7} bar are required for nucleation and growth of micrometer-sized grains in timescales relevant to stellar outflows. In addition, small-scale heterogeneities with higher densities are likely to be present in circumstellar outflows (e.g., Woitke and Niccolini, 2005; Redman et al., 2003). At such high pressures ($>10^{-7}$ bar), our experiments may provide information about the conditions of dust formation in circumstellar shells. They show that condensation at high-temperature could result in direct formation of crystalline grains, rather than amorphous silicates formed at high-supercooling, and later annealed in specific conditions (e.g., in high-mass loss stars, Kozasa and Sogawa, 1997). The direct condensation of forsterite, spinel, corundum, or diopside would explain the crystalline features of IR spectra of evolved stars. However, the presence of both crystalline and amorphous silicates in circumstellar dust shells implies that Mg and Si condensation has not uniquely taken place by such high-temperature near-equilibrium condensation processes, and/or that initially crystalline grains are rapidly amorphized by stellar radiation (e.g., Bradley, 1994; Carrez et al., 2002).

Our experimental condensates from a proxy of the solar gas reproduce the crystallinity and the mineralogy of most oxygen-rich presolar grains (e.g., Nittler et al., 1994, 1997; Huss et al., 1994; Choi et al., 1998, 1999; Stroud et al., 2002; Messenger et al., 2003), which suggests that these grains may have formed by high-temperature condensation. However, kinetics probably also plays a role in the

mineralogy of these circumstellar grains. The high abundance of corundum among presolar grains, which is at variance with its relative rarity in meteorites, suggests such kinetics effects. Our experiments show that the reaction of corundum with the gas to produce spinel is rapid. The survival of large presolar grains of corundum in stellar outflows therefore implies that they have been preserved from back reaction with the gas phase, either because of very rapid cooling, rapid density decrease or by physical removal. In addition, our results suggest that in order to be of micrometric size and preserved from back reaction with the gas phase, they should have grown at very high temperature, far above the stability field of spinel (e.g., $T > 1228$ °C at $P_T = 10^{-3}$ bar, Ebel and Grossman, 2000). The observation that some presolar spinels or corundums are non-stoichiometric (Choi et al., 1998; Zinner et al., 2005) suggests that some corundum grains did begin to react with the gas phase before their removal. Finally, C-rich presolar grains show unexpected amorphous rims (e.g., Croat et al., 2003), such as those observed on our condensates (Figs. 8 and 18). Although an origin of these rims by sputtering has been proposed, an origin by the condensation process itself must now be considered.

6. Conclusions

Using the techniques of laser-ablation and nanoparticles evaporation, we have developed a new apparatus allowing us to perform the first successful near-equilibrium high-temperature condensation of multi-elemental refractory gases at low-pressure. Our experimental results show that high-temperature condensation of multi-elemental refractory gases (''Mg–Si-rich'' and $An_{50}Di_{50}$) at $\sim 4 \times 10^{-3}$ bar results in direct formation of crystalline grains, that condense either directly in the gas or on the Pt-grid. The condensation of amorphous phases with stochastic composition is thus not favored.

The mineralogy of the condensed crystals, close to that predicted by equilibrium thermodynamic calculations, varies with temperature and duration of the condensation experiments. We have shown that chemical reactions between gas and condensates are rapid enough to attain a steady state on a relatively short period of time ($\sim$1 h at $\sim 4 \times 10^{-3}$ bar). Furthermore, high-temperature condensation results in chemical fractionation of the gas, i.e. depletion in refractory elements at high-temperature. This experimental work also reveals that condensation of some phases such as spinel may be kinetically favored.

This experimental study demonstrates that the non-igneous CAIs could have formed by high-temperature condensation in the early nebula. It also shows that crystalline grains can be formed in the outflows of evolved stars by high-temperature condensation. However, our experimental work indicates that the mineralogy of such condensed material, as well as the pressure–temperature conditions in their stellar environments cannot be completely understood without taking into account the influence of kinetics.

Acknowledgments

We are indebted to L. Zimmerman for its technical help in the design and building of the apparatus. We also thank A. Rouiller and A. Mulot for their help in building the apparatus. We are grateful to A. Kölher and S. Barda for assistance with the electron microprobe and SEM at the Service d'Analyses of the Université Henri Poincaré, Nancy (France). Jikta Lhomme and Luc Marin are also thanked with help in chemistry. A.T. greatly thanks Jérôme Aléon and Etienne Deloule for discussions. The authors are very grateful to the Associate Editor A.N. Krot and to D. Ebel and M. Petaev for their very detailed and helpful reviews that greatly improved our manuscript. This work was supported by INSU through PNP and PCM1 grants (G.L. and F.R.). This is CRPG contribution No. 1820.

Associate editor: Alexander N. Krot

References

Abraham, F.F., 1974. *Homogeneous Nucleation Theory*. Academic Press, New York, p. 263.

Aléon, J., Krot, A.N., McKeegan, K.D., 2002. Calcium–aluminium-rich inclusions and amoeboid olivine aggregates from the CR carbonaceous chondrites. *Meteorit. Planet. Sci.* **37**, 1729–1755.

Amelin, Y., Krot, A.N., Hutcheon, I.D., Ulyanov, A.A., 2002. Lead isotopic ages of chondrules and calcium–aluminium-rich inclusions. *Science* **297**, 1678–1683.

Anders, E., Grevesse, N., 1989. Abundances of the elements: meteoritic and solar. *Geochim. Cosmochim. Acta* **53**, 197–214.

Arrhenius, G., Alfvén, H., 1971. Fractionation and condensation in space. *Earth Planet. Sci. Lett.* **10**, 253–267.

Barshay, S.S., Lewis, J.S., 1976. Chemistry of primitive solar material. *Ann. Rev. Astr.* **14**, 81–94.

Beckett, J.R., Grossman, L., 1988. The origin of type C inclusions from carbonaceous chondrites. *Earth Planet. Sci. Lett.* **89**, 1–14.

Bernatowicz, T.J., Cowsik, R., 1997. Conditions in stellar outflows inferred from laboratory studies of presolar grains. In: Bernatowicz, T.J., Zinner, E.K. (Eds.), *Astrophysical Implications of the Laboratory Study of Presolar Materials*. AIP, Woodbury, NY, USA, pp. 391–423.

Bernatowicz, T.J., Cowsik, R., Gibbons, P.C., Lodders, K., Fegley Jr., B., Amari, S., Lewis, R.S., 1996. Constraints on stellar grain formation from presolar graphite in the Murchison meteorite. *Astrophys. J.* **472**, 760–782.

Bischoff, A., Palme, H., 1987. Composition and mineralogy of refractory-metal-rich assemblages from a Ca, Al-rich inclusion in the Allende meteorite. *Geochim. Cosmochim. Acta* **51**, 2733–2748.

Blander, M., Fuchs, L.H., 1975. Calcium–aluminium-rich inclusions in the Allende meteorite: evidence for a liquid origin. *Geochim. Cosmochim. Acta* **39**, 1605–1619.

Blander, M., Katz, J.L., 1967. Condensation of primordial dust. *Geochim. Cosmochim. Acta* **31**, 1025–1034.

Boynton, W.V., 1975. Fractionation in the solar nebula: condensation of yttrium and the rare earth elements. *Geochim. Cosmochim. Acta* **39**, 569–584.

Bradley, J.P., 1994. Chemically anomalous, preaccretionally irradiated grains in interplanetary dust from comets. *Science* **265**, 925–929.

Bradley, J.P., Brownlee, D.E., Veblen, D.R., 1983. Pyroxene whiskers and platelets in interplanetary dust: evidence of vapour phase growth. *Nature* **301**, 473–477.

Buffat, Ph., Borel, J.-P., 1976. Size effect on the melting temperature of gold particles. *Phys. Rev. A* **13**, 2287–2298.

Cameron, A.G.W., Fegley, M.B., 1982. Nucleation and condensation in the primitive solar nebula. *ICARUS* **52**, 1–13.

Carrez, P., Demyk, K., Cordier, P., Gengembre, L., Grimblot, J., d'Hendecourt, L., Jones, A.P., Leroux, H., 2002. Low-energy helium ion irradiation-induced amorphization and chemical changes in olivine: insights for silicate dust evolution in the interstellar medium. *Meteorit. Planet. Sci.* **37**, 1599–1614.

Chen, L.-C., 1994. Particulates generated by pulsed laser ablation. In: Chrisey, D.B., Hubler, G.K. (Eds.), *Pulsed Laser Deposition of Thin Films*. John Wiley & Sons, New-York, pp. 167–198.

Choi, B-G., Huss, G.R., Wasserburg, G.J., Gallino, R., 1998. Presolar corundum and spinel in ordinary chondrites: origins from AGB stars and a supernova. *Science* **282**, 1284–1289.

Choi, B-G., Wasserburg, G.J., Huss, G.R., 1999. Circumstellar hibonite and corundum and nucleosynthesis in asymptotic giant branch stars. *Astrophys. J.* **522**, L133–L136.

Christophe Michel-Lévy, M., 1968. Un chondre exceptionnel dans la meteorite de Vigarano. *Bull. Soc. Fr. Minéral. Cristallogr.* **91**, 212–214.

Christophe Michel-Lévy, M., 1981. Some clues to the history of the H-group chondrites. *Earth Planet. Sci. Lett.* **54**, 67–80.

Cliff, G., Lorimer, G.W., 1975. The quantitative analysis of thin-sections. *J. Microsc.* **103**, 203–207.

Croat, T.K., Bernatowicz, T., Amari, S., Messenger, S., Stadermann, F.J., 2003. Structural, chemical, and isotopic microanalytical investigations of graphite from supernovae. *Geochim. Cosmochim. Acta* **67**, 4705–4725.

Davis, A.M., MacPherson, G.J., Clayton, R.N., Mayeda, T.K., Sylvester, P.J., Grossman, L., Hinton, R.W., Laughlin, J.R., 1991. Melt solidification and late-stage evaporation in the evolution of a FUN inclusion from the Vigarano C3V chondrite. *Geochim. Cosmochim. Acta* **55**, 621–637.

Day, K.L., Donn, B., 1978. An experimental investigation of the condensation of silicate grains. *Astrophys. J.* **222**, L45–L48.

Demyk, K., Dartois, E., Wiesemeyer, H., Jones, A.P., d'Hendecourt, L., 2000. Structure and chemical composition of the silicate dust around OH/IR stars. *Astron. Astrophys.* **364**, 170–178.

Dominik, C., Sedlmayr, E., Gail, H.-P., 1993. Dust formation in stellar winds. VI. Moment equations for the formation of heterogeneous and core-mantle grains. *Astron. Astrophys.* **277**, 578–594.

Draine, B.T., 1979. Time-dependent nucleation theory and the formation of interstellar grains. *Astrophys. Space Sci.* **65**, 313–335.

Ebel, D.S., 2000. Variations on solar condensation: sources of interstellar dust nuclei. *J. Geophys. Res.* **105** (A5), 10363–10370.

Ebel, D.S., Grossman, L., 2000. Condensation in dust-enriched systems. *Geochim. Cosmochim. Acta* **64**, 339–366.

Fabian, D., Jäger, C., Henning, Th., Dorschner, J., Mutschke, H., 2000. Steps toward interstellar silicate mineralogy. V. Thermal evolution of amorphous magnesium silicates and silica. *Astron. Astrophys.* **364**, 282–292.

Fabian, D., Posch, Th., Mutschke, H., Kerschbaum, F., Dorschner, J., 2001. Infrared optical properties of spinels. A study of the carrier of the 13, 17 and 32 μm emission features observed in ISO-SWS spectra of oxygen-rich AGB stars. *Astron. Astrophys.* **373**, 1125–1138.

Fegley Jr., B., 2000. Kinetics of gas-grain reactions in the solar nebula. *Space Sci. Rev.* **92**, 177–200.

Fegley, B., Post, J.E., 1985. A refractory inclusion in the Kaba CV3 chondrite—some implications for the origin of spinel-rich objects in chondrites. *Earth Planet. Sci. Lett.* **75**, 297–310.

Fegley Jr., B., Prinn, R.G., 1989. Solar nebula chemistry: implications for volatiles in the solar system. In: *The Formation and Evolution of Planetary Systems*. Cambridge University Press, Cambridge, England, pp. 171–211.

Field, G.B., 1974. Interstellar abundances: gas and dust. *Astrophys. J.* **187**, 453–459.

Fix, J.D., 1970. Some possible components of circumstellar grain material. *Astrophys. J.* **161**, 359–360.

Gail, H.-P., Sedlmayr, E., 1986. The primary condensation process for dust around late M-type stars. *Astron. Astrophys.* **166**, 225–236.

Gail, H.-P., Sedlmayr, E., 1987. Dust formation in stellar winds. In: Morfill, G.E., Scholer, M. (Eds.), *Physical Processes in Interstellar Clouds*. D. Reidel Publishing Company, Dordrecht, Holland, pp. 275–303.

Gail, H.-P., Sedlmayr, E., 1999. Mineral formation in stellar winds. I. Condensation sequence of silicate and iron grains in stationary oxygen rich outflows. *Astron. Astrophys.* **347**, 594–616.

Gehrz, R.D., 1989. Sources of stardust in the galaxy. In: Allamandola, L.J., Tielens, A.G.G.M. (Eds.), *Interstellar Dust*, IAU 135. Kluwer Academic Publishers, Dordrecht, Holland, pp. 445–453.

Gilman, R.C., 1969. On the composition of circumstellar grains. *Astrophys. J.* **155**, L185–L187.

Givargizov, E.I., 1987. Highly anisotropic crystals. In: Senechal, M. (Ed.), Kluwer Academic Publishers, Dordrecht, Holland, p. 395.

Gnedovets, A.G., Kul'batskii, E.B., Smurov, I., Flamant, G., 1996. Particles synthesis in erosive laser plasma in a high pressure atmosphere. *Appl. Surf. Sci.*, 272–279.

Gray, C.M., Papanastassiou, D.A., Wasserburg, G.J., 1973. The identification of early condensates from the solar nebula. *ICARUS* **20**, 213–239.

Grossman, L., 1972. Condensation in the primitive solar nebula. *Geochim. Cosmochim. Acta* **36**, 597–619.

Grossman, L., 1975. Petrography and mineral chemistry of Ca-rich inclusions in the Allende meteorite. *Geochim. Cosmochim. Acta* **39**, 433–454.

Grossman, L., Steele, I.M., 1976. Amoeboid olivine aggregates in the Allende meteorite. *Geochim. Cosmochim. Acta* **40**, 149–155.

Grossman, L., Ebel, D.S., Simon, S.B., Davis, A.M., Richter, F.M., Parsad, N.M., 2000. Major element chemical and isotopic compositions of refractory inclusions in C3 chondrites: the separate roles of condensation and evaporation. *Geochim. Cosmochim. Acta* **64**, 2879–2894.

Grossman, L., Ebel, D.S., Simon, S.B., 2002. Formation of refractory inclusions by evaporation of condensate precursors. *Geochim. Cosmochim. Acta* **66**, 145–161.

Hirth, J.P., Pound, G.M., 1963. *Condensation and Evaporation*. Pergamon Press, Oxford, p. 192.

Huss, G.R., Fahey, A.J., Gallino, R., Wasserburg, G.J., 1994. Oxygen isotopes in circumstellar Al_2O_3 grains from meteorites and stellar nucleosynthesis. *Astrophys. J.* **430**, L81–L84.

Itoh, S., Kojima, H., Yurimoto, H., 2004. Petrography and oxygen isotopic compositions in refractory inclusions from CO chondrites. *Geochim. Cosmochim. Acta* **68**, 183–194.

Kemper, F., de Koter, A., Waters, L.B.F.M., Bouwman, J., Tielens, A.G.G.M., 2002. Dust and the spectral energy distribution of the OH/IR star OH 127.8 + 0.0: evidence for circumstellar metallic iron. *Astron. Astrophys.* **384**, 585–593.

Komatsu, M., Krot, A.N., Petaev, M.I., Ulyanov, A.A., Keil, K., Miyamoto, M., 2001. Mineralogy and petrography of amoeboid olivine aggregates from the reduced CV3 chondrites Efremovka, Leoville and Vigarano: products of nebular condensation, accretion and annealing. *Meteorit. Planet Sci.* **36**, 629–641.

Kornacki, A.S., Wood, J.A., 1985. Mineral chemistry and origin of spinel-rich inclusions in the Allende CV3 chondrite. *Geochim. Cosmochim. Acta* **49**, 1219–1237.

Kozasa, T., Sogawa, H., 1997. Formation of dust grains in circumstellar envelopes of oxygen-rich AGB stars. *Astrophys. Space Sci.* **251**, 165–170.

Krot, A.N., MacPherson, G.J., Ulyanov, A.A., Petaev, M.I., 2004a. Fine-grained, spinel-rich inclusions from the reduced CV chondrites Efremovka and Leoville: I. Mineralogy, petrology, and bulk chemistry. *Meteorit. Planet. Sci.* **39**, 1517–1553.

Krot, A.N., Petaev, M.I., Russel, S.S., Itoh, S., Fagan, T.J., Yurimoto, H., Chizmadia, L., Weisberg, M.K., Komatsu, M., Ulyanov, A.A., Keil, K., 2004b. Amoeboid olivine aggregates and related objects in

carbonaceous chondrites: records of nebular and asteroid processes. *Chem. Erde* **64**, 185–239.

Larimer, J.W., 1967. Chemical fractionations in meteorites-I. Condensation of the elements. *Geochim. Cosmochim. Acta* **31**, 1215–1238.

Larimer, J.W., Anders, E., 1970. Chemical fractionations in meteorites-III. Major element fractionations in chondrites. *Geochim. Cosmochim. Acta* **34**, 367–387.

Larimer, J.W., Bartholomay, M., 1979. The role of carbon and oxygen in cosmic gases—some applications to the chemistry and mineralogy of enstatite chondrites. *Geochim. Cosmochim. Acta* **43**, 1455–1466.

Lattimer, J.M., Schramm, D.N., Grossman, L., 1978. Condensation in supernova ejecta and isotopic anomalies in meteorites. *Astrophys. J.* **219**, 230–249.

Lewis, J.S., 1974. The temperature gradient in the solar nebula. *Science* **186**, 440–443.

Lin, Y., Kimura, M., 2003. Ca–Al-rich inclusions from the Ningqiang meteorite: continuous assemblages of nebular condensates and genetic link to Type B inclusions. *Geochim. Cosmochim. Acta* **67**, 2251–2267.

Lodders, K., Fegley Jr., B., 1997. Condensation chemistry of carbon stars. In: Bernatowicz, T.J., Zinner, E.K. (Eds.), *Astrophysical Implications of the Laboratory Study of Presolar Materials*. AIP, Woodbury, NY, USA, pp. 391–423.

Lord III, H.C., 1965. Molecular equilibria and condensation in a solar nebula and cool stellar atmospheres. *ICARUS* **4**, 279–288.

MacPherson, G.J., 2004. Calcium–aluminium rich inclusions in chondritic meteorites. In: Davis, A.M., et Holland, H.D. (Eds.), *Treatise on Geochemistry Volume 1: Meteorites, Comets and Planets*. Elsevier, Oxford, pp. 201–246.

MacPherson, G.J., Davis, A.M., 1993. A petrologic and ion microprobe study of a Vigarano Type B refractory inclusion: evolution by multiple stages of alteration and melting. *Geochim. Cosmochim. Acta* **57**, 231–243.

MacPherson, G.J., Davis, A.M., 1994. Refractory inclusions in the prototypical CM chondrite, Mighei. *Geochim. Cosmochim. Acta* **58**, 5599–5625.

MacPherson, G.J., Grossman, L., 1984. "Fluffly" type A Ca-, Al-rich inclusions in the Allende meteorite. *Geochim. Cosmochim. Acta* **48**, 29–46.

MacPherson, G.J., Bar-Matthews, M., Tanaka, T., Olsen, E., Grossman, L., 1983. Refractory inclusions in the Murchison meteorite. *Geochim. Cosmochim. Acta* **47**, 823–839.

MacPherson, G.J., Wark, D.A., Armstrong, J.T., 1988. Primitive material surviving in chondrites: refractory inclusions. In: Kerridge, J.F., Matthews, M.S. (Eds.), *Meteorites and the early Solar System*. pp. 747–807.

Marine, W., Patrone, L., Luk'yanchuk, B., Sentis, M., 2000. Strategy of nanocluster and nanostructure synthesis by conventional pulsed laser ablation. *Appl. Surf. Sci.*, 345–352.

Marvin, U.B., Wood, J.A., Dickey Jr., J.S., 1970. Ca–Al rich phases in the Allende meteorite. *Earth Planet. Sci. Lett.* **7**, 346–350.

McGuire, A.V., Hashimoto, A., 1989. Origin of zoned fine-grained inclusions in the Allende meteorite. *Geochim. Cosmochim. Acta* **53**, 1123–1133.

Messenger, S., Keller, L.P., Stadermann, F.J., Walker, R.M., Zinner, E., 2003. Samples of stars beyond the solar system: silicate grains in interplanetary dust. *Science* **300**, 105–108.

Molster, F.J., Waters, L.B.F.M., Trams, N.R., Van Winckel, H., Decin, L., Van Loon, J.Th., Jäger, C., Henning, Th., Käufl, H.-U., De Koter, A., Bouwman, J., 1999. The composition and nature of the dust shell surrounding the binary AFGL 4106. *Astron. Astrophys.* **350**, 163–180.

Molster, F.J., Waters, L.B.F.M., Tielens, A.G.G.M., 2002. Crystalline silicate dust around evolved stars. II. The crystalline silicate complexes. *Astron. Astrophys.* **382**, 222–240.

Nagahara, H., Kushiro, I., Mysen, B.O., Mori, H., 1988. Experimental vaporization and condensation of olivine solid solution. *Nature* **331**, 516–518.

Nagashima, K., Krot, A.N., Yurimoto, H., 2004. Stardust silicates from primitive meteorites. *Nature* **428**, 921–924.

Nittler, L.R., Alexander, C.M.O'D., Gao, X., Walker, R.M., Zinner, E.K., 1994. Interstellar oxide grains from the Tieschitz ordinary chondrite. *Nature* **370**, 443–446.

Nittler, L.R., Alexander, C.M.O'D., Gao, X., Walker, R.M., Zinner, E., 1997. Stellar sapphires: the properties and origins of presolar Al_2O_3 in meteorites. *Astrophys. J.* **483**, 475–495.

Nuth, J.A., Donn, B., 1982. Experimental studies of the vapor phase nucleation of refractory compounds. I. The condensation of SiO. *J. Chem. Phys.* **77**, 2639–2646.

Nuth, J.A., Donn, B., 1983. Experimental studies of the vapor phase nucleation of refractory compounds. II. The condensation of an amorphous magnesium silicate. *J. Chem. Phys.* **78**, 1618–1620.

Nuth III, J.A., Hallenbeck, S.L., Rietmeijer, F.J.M., 2000. Laboratory studies of silicate smokes: analog studies of circumstellar materials. *J. Geophys. Res.* **105** (A5), 10387–10396.

Palme, H., 2000. Are there chemical gradients in the inner solar system? *Space Sci. Rev.* **192**, 237–262.

Petaev, M.I., Wood, J.A., 1998. The condensation with partial isolation (CWPI) model of condensation in the solar nebula. *Meteorit. Planet. Sci.* **33**, 1123–1137.

Podosek, F.A., Zinner, E.K., MacPherson, G.J., Lundberg, L.L., Brannon, J.C., Fahey, A.J., 1991. Correlated study of initial $^{87}Sr/^{86}Sr$ and Al–Mg isotopic systematics and petrologic properties in a suite of refractory inclusions from the Allende meteorite. *Geochim. Cosmochim. Acta* **55**, 1083–1110.

Qi, Y., Tahir, C., Johnson, W.L., Goddard III, W.A., 2001. Melting and crystallization in Ni nanoclusters: the mesoscale regime. *J. Chem. Phys.* **115**, 385–394.

Redman, M.P., Viti, S., Cau, P., Williams, D.A., 2003. Chemistry and clumpiness in planetary nebulae. *Mon. Not. R. Astron. Soc.* **345**, 1291–1296.

Richter, F.M., Davis, A.M., Ebel, D.S., Hashimoto, A., 2002. Elemental and isotopic fractionation of type B calcium-, aluminium-rich inclusions: experiments, theoretical considerations, and constraints on their thermal evolution. *Geochim. Cosmochim. Acta* **66**, 521–540.

Rietmeijer, F.J.M., Nuth III, J.A., Karner, J., 1999. Metastable eutectic condensation in a Mg–Fe–SiO–H_2–O_2 vapor: analogs to circumstellar dust. *Astrophys. J.* **527**, 395–404.

Rietmeijer, F.J.M., Hallenbeck, S.L., Nuth III, J.A., Karner, J., 2002. Amorphous magnesiosilicate smokes annealed in vacuum: the evolution of magnesium silicates in circumstellar and cometary dust. *ICARUS* **156**, 269–286.

Salpeter, E.E., 1977. Formation and destruction of dust grains. *Ann. Rev. Astron. Astrophys.* **15**, 267–293.

Savage, B.D., Sembach, K.R., 1996. Interstellar abundances from absorption-line observations with the Hubble Space Telescope. *Ann. Rev. Astron. Astrophys.* **34**, 279–329.

Sedlmayr, E., 1989. Dust condensation in stellar outflows. In: Allamandola, L.J., Tielens, A.G.G.M., (Eds.), *Interstellar Dust*, IAU 135. Kluwer Academic Publishers, Dordrecht, Holland, pp. 467–477.

Sedlmayr, E., Krüger, D., 1997. Formation of dust particles in cool stellar outflows. In: Bernatowicz, T.J., Zinner, E.K. (Eds.), *Astrophysical Implications of the Laboratory Study of Presolar Materials*. AIP, Woodbury, NY, USA, pp. 391–423.

Seinfeld, J.H., Pandis, S.N., 1998. *Atmospheric chemistry and physics*. Wiley-Interscience Publication, John Wiley and Sons, New-York, USA, p. 1326.

Sharp, C.M., Wasserburg, G.J., 1995. Molecular equilibria and condensation temperatures in carbon-rich gases. *Geochim. Cosmochim. Acta* **59**, 1633–1652.

Simon, S.B., Davis, A.M., Grossman, L., 1999. Origin of compact type A refractory inclusions from CV3 carbonaceous chondrites. *Geochim. Cosmochim. Acta* **63**, 1233–1248.

Stephens, J.R., Kothari, B.K., 1978. Laboratory analogues to cosmic dust. *Moon Planets* **19**, 139–152.

Stolper, E., 1982. Crystallization sequences of Ca–Al-rich inclusions from Allende: an experimental study. *Geochim. Cosmochim. Acta* **46**, 2159–2180.

Stroud, R.M., Nittler, L.R., Alexander, C.M.O'D., 2002. Transmission electron microscopy of a presolar corundum grain. *Meteorit. Planet. Sci.* **37**, A137.

Sylvester, P.J., Simon, S.B., Grossman, L., 1993. Refractory inclusions from the Leoville, Efremovka, and Vigarano C3V chondrites: major element differences between Types A and B, and extraordinary refractory siderophile element compositions. *Geochim. Cosmochim. Acta* **57**, 3763–3784.

Tielens, A.G.G.M., Allamandola, L.J., 1987. Evolution of interstellar dust. In: Morfill, G.E., Scholer, M. (Eds.), *Physical Processes in Interstellar Clouds*. Holland, Dordrecht, pp. 333–376.

Tielens, A.G.G.M., Waters, L.B.F.M., Molster, F.J., Justtanont, K., 1998. Circumstellar silicate mineralogy. *Astrophys. Space Sci.* **255**, 415–426.

Tissandier, L., Libourel, G., Robert, F., 2002. Gas–melt interactions and their bearing on chondrule formation. *Meteorit. Planet. Sci.* **37**, 1377–1389.

Toppani, A., Libourel, G., Robert, F., Ghambaja, J., Zimmermann, L., 2004. Synthesis of refractory minerals by high-temperature condensation of a gas of solar composition. *Lunar Planet. Sci.* **XXXV**, 1726.

Toppani, A., Robert, F., Libourel, G., de Donato, P., Barres, O., d'Hendecourt, L., Ghanbaja, J., 2005. A 'dry' condensation origin for circumstellar carbonates. *Nature* **437**, 1121–1124.

Urey, H.C., 1952. *The Planets*. Yale University Press, New Haven, CT.

Wark, D.A., Lovering, J.F., 1982. The nature and origin of type B1 and B2 Ca–Al-rich inclusions in the Allende meteorite. *Geochim. Cosmochim. Acta* **46**, 2581–2594.

Waters, L.B.F.M., Molster, F.J., de Jong, T., et al., 1996. Mineralogy of oxygen-rich dust shells. *Astron. Astrophys.* **315**, L361–L364.

Wautelet, M., 2005. On the melting of polyhedral elemental nanosolids. *Eur. Phys. J. Appl. Phys.* **29**, 51–54.

Weisberg, M.K., Connolly Jr., H.C., Ebel, D.S., 2004. Petrology and origin of amoeboid olivine aggregates in CR chondrites. *Meteorit. Planet. Sci.* **39**, 1741–1753.

Weisberg, M.K., Zolensky, M.E., Prinz, M., 1997. Fayalitic olivine in matrix of the Krymka LL3.1 chondrite: vapor-solid growth in the solar nebula. *Meteorit. Planet. Sci.* **32**, 791–801.

Wiechert, U., Hoefs, J., 1995. An eximer laser-based micro-analytical preparation technique for in-situ oxygen isotope analysis of silicate and oxide minerals. *Geochim. Cosmochim. Acta* **59**, 4093–4101.

Woitke, P., Niccolini, 2005. Dust cloud formation in stellar environments. II. Two-dimensional models for structure formation around AGB stars. *Astron. Astrophys.* **433**, 1101–1115.

Wood, J.A., Hashimotom, A., 1993. Mineral equilibrium in fractionated nebular systems. *Geochim. Cosmochim. Acta* **57**, 2377–2388.

Woolf, N.J., Ney, E.P., 1969. Circumstellar infrared emission from cool stars. *Astrophys. J.* **155**, L181–L184.

Yoneda, S., Grossman, L., 1995. Condensation of $CaO–MgO–Al_2O_3–SiO_2$ liquids from cosmic gases. *Geochim. Cosmochim. Acta* **59**, 3413–3444.

Zhang, Z., Lagally, M.G., 1997. Atomistic processes in the early stages of thin-film growth. *Science* **276**, 377–383.

Zinner, E., Nittler, L.R., Hoppe, P., Gallino, R., Straniero, O., Alexander, C.M.O'D., 2005. Oxygen, magnesium and chromium isotopic ratios of presolar spinel grains. *Geochim. Cosmochim. Acta* **69**, 4149–4165.